Plant wax isotopic reconstructions reveal thermodynamic drivers of hydroclimate over the last two glacial cycles at Great Salt Lake and Bear Lake, Utah

Rachel T. So[1*], Daniel E. Ibarra[2], Jessica E. Tierney[3], Elliot Jagniecki[4], Tim K. Lowenstein[5], Adam B. Jost[6], Kristian Olson[7], David McGee[6], and Sarah J. Feakins[1]

[1]Department of Earth Sciences, University of Southern California, Los Angeles, CA 90089, USA.

[2]Department of Earth, Environmental and Planetary Science, Brown University, Providence, RI 02906, USA.

[3]Department of Geoscience, University of Arizona, Tucson, AZ 85721, USA.

[4]Utah Geological Survey, Salt Lake City, UT 84114, USA.

[5]Department of Earth Sciences, Binghamton University, Binghamton, NY 13902, USA.

[6]Department of Earth, Atmospheric, and Planetary Sciences, Massachusetts Institute of Technology, Cambridge, MA, USA

[7]Department of Geology, Alfred University, Alfred, NY, USA

Corresponding author: Rachel T. So (rtso@usc.edu)

Key Points:

- Two large lakes in Utah yield leaf wax precipitation isotope reconstructions spanning more than two glacial-interglacial cycles.
- Precipitation isotope reconstructions align with most regional records and indicate coherent, large-scale regional hydroclimate changes.
- Thermodynamic processes best explain coherent changes in precipitation isotopes across the southwestern U.S.

Abstract

The growth and decay of the Laurentide ice sheet altered the hydrological cycle over southwestern North America. While it is well-documented that the last glacial was wetter and had isotopically lighter precipitation, much less information is available for prior glacials. Increased proxy coverage is needed to test climate models' ability to reconstruct these changes and to assess their predictive power for water availability in response to future climate change. Here, we present parallel precipitation isotope records spanning the last two glacial cycles from two large, proximal lakes in Utah, USA: Great Salt Lake and Bear Lake. We use plant wax *n*-alkane δD as a proxy for precipitation δD (δD_{precip}) and find coherent glacial-interglacial fluctuations in δD_{precip}, with a ~30‰ D-depletion during glacial maxima relative to interglacials. We find similar δD_{precip} values between the Holocene and Eemian, but at the lower-pCO_2 MIS 7 interglacial, D-enrichment is only weakly recorded at Great Salt Lake and absent at higher elevation Bear Lake. Comparison to regional proxy archives finds large-scale coherence in regional hydroclimate change over the last two glacial cycles is best explained by thermodynamic processes, with increased rainout efficiency, isotopic fractionation, and snow in a colder atmosphere. Comparison of proxies to climate model experiments showed models considerably underestimate glacial lowering of precipitation isotopic values, but overestimate inland Rayleigh distillation. New and assembled proxy reconstructions provide greater temporal and spatial coverage as targets for model skill in capturing hydroclimate variations across the past two glacial cycles.

Plain Language Summary

Lakes preserve sedimentary histories of climate near where people live. We studied climate histories from two large lakes, Great Salt Lake and Bear Lake in Utah, USA. Drill-cores from these two lakes have sediments that span the last 240,000 years, covering two glacial cycles. These cores collected in 2000 provide rare archives of long-term climate history preserved in continental settings. This dual-deep-drilled record of two neighboring lakes is globally unique, allowing us to compare the record contained within Great Salt Lake that has historically expanded into a much larger lake, the remnants of which are visible as the Bonneville salt flats, with a record from Bear Lake, a fresher lake at higher elevation. We analyze wax molecules from plant leaves that blew into the lakes and were preserved in lake sediments. These molecules

contain signals of past rainfall patterns across two large climate swings, with synchronous changes in rainfall recorded by the two lakes. We compare these rainfall records with several other lake and cave records in the region that also show similar patterns, providing confidence in regional changes. Studying how mid-continental rainfall patterns changed in the past helps us understand the response of rainfall to climate change.

Keywords: plant wax; hydroclimate; last glacial; last interglacial; MIS 7; stable isotopes

1. Introduction

Proxy records from southwestern North America suggest a much wetter climate in the last glacial period, particularly during the glacial termination, relative to today. Deep, expansive lakes such as Lake Lahontan and Lake Bonneville occupied large portions of the Great Basin across Nevada and Utah, USA (Broecker and Kaufman, 1965; Oviatt et al., 1992; Reheis, 1999). Farther south, lakes also experienced pluvial highstands during the last two glacial terminations including at Owens Lake, Lake Manly, Searles Lake, and Lake Elsinore (Benson et al., 1996; Kirby et al., 2013; Lowenstein et al., 2024; Menking et al., 1997; Peaple et al., 2022) and speleothems, like those from Devils Hole, recorded elevated water tables (Wendt et al., 2018). Many proxy archives capture evidence for a regionally expansive glacial pluvial (e.g., Lowenstein et al., 2024; Reheis et al., 2014), and many others record the isotopic composition of precipitation (Asmerom et al., 2010; Feakins et al., 2019; Lachniet et al., 2014; Oster et al., 2009; Peaple et al., 2022; Winograd et al., 1992).

Precipitation isotopic records are powerful, complex tracers of hydroclimate that incorporate several processes, the combination of which generally result in lower values in glacial intervals. Early work by Dansgaard (1964) identified temperature as a major control of precipitation isotopic signatures in mid- to high latitudes. Equilibrium fractionation at colder condensation temperatures along with proportionally greater condensation into the solid phase rather than liquid phase (i.e., snow rather than rain) both lead to a depletion in heavy isotopes (^{18}O and D). Changes in the amount of integrated upstream rainout (Rayleigh distillation), also influence precipitation isotopic composition. Greater rainout lowers isotopic values, which is expected in colder climate states because of the greater cooling of land relative to oceans and as a colder atmosphere can hold less moisture by the Clausius-Clapeyron relation. Storm track changes

84 further modify precipitation isotopes through shifts in moisture sources and rainout pathways
85 (distance inland and topography). Laurentide ice sheet-driven southward shift and strengthening
86 of the midlatitude jet during the Last Glacial Maximum (LGM) (Fu, 2023; Oster et al., 2015),
87 and more intense atmospheric river activity during the glacial termination, specifically Heinrich
88 Stadial 1 (McGee et al., 2018; Oster et al., 2023), have all been suggested to explain glacial
89 pluvials in the southwestern U.S. Greater moisture has also been attributed to a combination of
90 thermodynamic and dynamic mechanisms, including more efficient moisture removal from the
91 atmosphere (Tabor et al., 2021) or greater moisture advection into the region (Morrill et al.,
92 2018) as a result of steeper land-sea temperature gradients.

93 To better understand the hydroclimate over glacial-interglacial cycles, continental precipitation
94 isotope reconstructions are invaluable, yet regional records fully encompassing multiple glacial
95 cycles are limited to a few speleothem (Lachniet, 2016; Moseley et al., 2016) and lacustrine
96 records (Peaple et al., 2022). Here, we generate and compare two new hydroclimate
97 reconstructions spanning two full glacial cycles from Great Salt Lake and Bear Lake. By
98 analyzing records from these two proximal but distinct lake systems, we have a unique
99 opportunity to compare the records against each other and ascertain reproducibility, eliminating
100 concerns over complications from lake basin differences. The two records expand on spatial
101 patterns of precipitation in the region as they are located at the boundary of the modern
102 precipitation dipole (between 40°N and 42°N) where the wet/dry direction of past and future
103 precipitation change is less certain (Wise, 2010).

104 ### 1.1. Study location: lake basins, catchment and vegetation

105 Great Salt Lake and Bear Lake are two mid-latitude lakes located 120 km apart in the
106 northeastern-most region of the Great Basin in the western United States (**Figure 1a**). Despite
107 their proximity, the lakes differ markedly; Great Salt Lake is a hypersaline terminal lake and
108 Bear Lake is a smaller, brackish to freshwater lake. They were at times connected by the Bear
109 River, with Great Salt Lake serving as the terminus of the Bear River drainage (Kaufman et al.,
110 2009) (**Figure 1c**). Bear Lake has alternated between open and closed basin conditions due to its
111 shifting connectivity to the Bear River (Kaufman et al., 2009), and previous studies have shown
112 that both lakes expanded and contracted in response to glacial-interglacial climate variability

(Balch et al., 2005; Kaufman et al., 2009; Laabs and Kaufman, 2003; Oviatt et al., 1999). Several deep lake cycles are evident at Great Salt Lake over the last 700 kyr, notably the "Lake Bonneville" highstand during the last glacial termination (Oviatt et al., 2015; Oviatt et al., 1999) (**Figure 1b**).

Great Salt Lake is located at 1,280 masl with a surface area of 4,100 km^2, maximum depth of 10 m, and a catchment area of 56,000 km^2 (Davis et al., 2022). The lake has three main river inflows–Bear River, Weber River, and Jordan River–with the majority coming from the Bear River (Davis et al., 2022). Around the lake, the vegetation is characterized as arid shrubland dominated by greasewood (*Sarcobatus*, ~1,300 m) with sagebrush (*Artemisia*) dominating above 1300 m (Davis, 1998). Between ~1900 and ~2,300 m, a mixed woodland-shrubland zone includes pine, juniper, and sagebrush, while fir and spruce forests occur on mountain slopes >2300 m.

Bear Lake is a montane lake situated at 1,805 masl with a surface area of 280 km^2, maximum depth of 63 m, and a catchment area of 1,300 km^2 (Kaufman et al., 2009). The Bear Lake catchment elevation range extends from 1,805 m to 3,800 m with distinct altitudinal vegetation zones. While much of the lake margin today is used for agricultural land or is urbanized, natural vegetation consists of sagebrush and desert shrubland in the lowlands around the lake (Jimenez-Moreno et al., 2007). Above the lowlands are forests of ponderosa pines, Rocky Mountain piñon and aspen, Utah juniper, and Douglas-fir (<2,500 m) followed by lodgepole pine (2,400–3,200 m). The upper slopes of the Uinta Mountains (>3,200 m) have subalpine Engelmann spruce and fir, and alpine tundra (Jackson et al., 2005).

1.2. Regional climate

The region surrounding both Great Salt Lake and Bear Lake experiences warm, dry summers and cool, wet winters, with the higher elevation Bear Lake being relatively colder and wetter (National Centers for Environmental Information, 2020a, b) (**Figure 2**). Most precipitation falls in winter and spring between November and April. We converted precipitation accumulations into snow water equivalent (SWE) based on the snow-to-liquid ratio (SLR) of 13 for the Wasatch Range (Veals et al., 2025), with snow amounting to 20%–30% of the annual precipitation. At Salt Lake City (UT) southeast of Great Salt Lake, monthly temperatures range from 0°C to 27°C

(National Centers for Environmental Information, 2020b) and monthly δD_{precip} ranges from -140‰ to -40‰ (Waterisotopes Database, 2025b) (**Figure 2a**). At Laketown (UT) south of Bear Lake, temperatures range from -5°C to 20°C (National Centers for Environmental Information, 2020a) and monthly δD_{precip} ranges from -160‰ to -50‰ (Waterisotopes Database, 2025a) (**Figure 2b**). NOAA HYSPLIT4 DJF and JJA 72-hr back trajectories of air masses at ~500 hPa indicate nearly all trajectories to the lakes are westerlies (archived trajectories for Dec 2019–Aug 2024; Rolph et al., 2017; Stein et al., 2015) (**Figure S1**). DJF trajectories feature westerlies and northerlies that originate from the mid to high latitude North Pacific, while JJA trajectories feature westerlies that originate from the mid to subtropical latitude North Pacific. These trajectories are in line with Friedman et al. (2002a) which found from 1991 to 1993, 87% of all precipitation to Cedar City (UT; 37.69°N, 113.08°W, 1,780 masl), 350 km southwest of Salt Lake City, was sourced from the Pacific Ocean.

2. Materials and methods

2.1. Lake sediment cores

As part of the Global Lakes Drilling Program (GLAD), sediment cores were collected from both lakes in 2000, with the deepest cores exceeding 120 m below lake floor (mblf) (Kelts et al., 2000). Both drilling locations reached sediments from marine isotope stage (MIS) 7, covering two full glacial cycles (Balch et al., 2005; Colman et al., 2006). These cores offer a unique opportunity to reconstruct hydroclimate over multiple glacial cycles, providing valuable information on glacial-interglacial climate beyond the last glacial limit of many lacustrine records.

At Great Salt Lake, five parallel cores, GLAD1-GSL00-4A, -4E, -4B, -4C, and -4D (arranged in order of depth; hereafter GLAD1-GSL00-4), were drilled, reaching a maximum penetration depth of 121 m (Palacios-Fest et al., 2000). The core site (41.13°N, 112.56°W) is 9.4 m deep and near the center of the lake. Most of the core consists of carbonate mud with two prominent evaporite crusts at depths of 11–14 m and 68–71 m. The upper crust is composed of thenardite (Na_2SO_4) underlain by ~1 m of dark sapropelic muds. The lower crust is halite (NaCl) underlain by ~4 m of dark-colored muds (Palacios-Fest et al., 2000). The two evaporite crusts likely formed during large a lake level drop following two recent deep lake cycles timed approximately

to the ends of the last two glacial periods (Balch et al., 2005). Balch et al. (2005) generated a core age model using radiocarbon-dated charcoal (n = 5) and one trichome sample, biostratigraphic correlations (n = 2), tephra dates (n = 2), and carbonate and evaporite uranium-series dates (n = 10). Age for the lower 100 m of the core was estimated from uranium-series dates at only three unique depths. The sparse number of samples in this section (n = 7) along with substantial age uncertainties (up to 20 kyr) prompted efforts to obtain more samples for uranium-series measurements in the lower portion of the core. This study uses a revised age model made with the R package Bacon (Blaauw and Christen, 2011), incorporating dates from Balch et al. (2005) and updated with 11 new samples dated by uranium-series (So et al., 2026) (**Figure S2**). The main changes between the Balch et al. (2005) and the updated GLAD1-GSL00-4 age models (So et al., 2026) are improved constraints around glacial termination 2 (T2) as well as a new bottom core age estimate of 235 ka. In addition, we note that compound specific radiocarbon dating on *n*-alkanes at a single depth in the Holocene has indicated that the pre-aging of plant waxes prior to deposition in the core may be on the order of 2 kyr (Bowen et al., 2019), which is unlikely to be significant for regional climate comparisons in these records spanning 235 ka.

At Bear Lake, two parallel cores, GLAD1-BL00-1D and -1E (hereafter GLAD1-BL00-1 for brevity), were drilled, reaching a maximum penetration depth of 120 m. The core site (41.95°N, 111.31°W) is 54.8 m deep, just west of the lake's depocenter, originally chosen to avoid mass wasting associated with faulting along the eastern margin (Kaufman et al., 2009). The cores consist mostly of carbonate-rich muds (Rosenbaum et al., 2000). Colman et al. (2006) generated a core age model using radiocarbon-dated pollen (n = 27), one magnetic excursion, one carbonate uranium-series age, and, in the bottom half of the core where no dates were measured, correlation to the Devils Hole speleothem $\delta^{18}O$ (8 tie points). For this study, we used all age measurements of Colman et al. (2006), except the Devils Hole tie points, to generate an updated age model using the R package Bacon (Blaauw and Christen, 2011), which produced a bottom core age of 240 ka (**Figure S3**).

The Bear Lake cores were sampled in May–June 2022 at the Continental Scientific Drilling (CSD) Facility at the University of Minnesota, Minneapolis. Samples (~20 g) were collected at ~1 m (~2 ka) intervals along the 120 m core, integrating 2 cm of depth (~40 yr), totaling 120

samples. The Great Salt Lake cores were sampled in Jan 2023 and May 2024 at CSD. Samples (~20 g) were collected approximately every 2 m (~4 ka) along the 121 m core, integrating 2 cm of depth (~40 yr), totaling 75 samples. Sediments from both cores were stored in a -20°C freezer until processing.

2.2. Lipid extraction and separation

Sediment samples were prepared using established procedures for biomarker extraction and purification as described by Peaple et al. (2022). After freeze-drying then homogenizing with a mortar and pestle, sediments were processed using Accelerated Solvent Extraction (Dionex ASE 350) with 9:1 DCM: MeOH at 100°C and 1500 psi for one 15-minute extraction cycle, yielding total lipid extracts (TLE). TLEs were separated over NH_2-coated silica gel columns, flash eluting the neutral fraction with 2:1 DCM:isopropanol and the acid fraction with 4% formic acid in ethyl ether. The neutral fraction was partitioned over 5% deactivated silica gel columns, flash eluting *n*-alkanes with hexanes. For sediments suspected to have been deposited under anoxic conditions, the alkane fraction was further cleaned using activated copper columns to remove elemental sulfur. The acid fraction was methylated with 95:5 MeOH:hydrochloric acid at 70˚C for 12 hours using methanol of known isotopic composition. Methylated products–fatty acid methyl esters (FAMEs)–were separated and dried over anhydrous sodium sulfate columns, and extracts were purified over 5% deactivated silica gel columns, eluting FAMEs with DCM. For stable isotope measurements, select alkanes and FAMEs fractions, containing closely eluting peaks of unsaturated compounds at the target compounds based on their gas chromatograms (see **Text S2**), were further cleaned using silver nitrate-coated silica gel columns, eluting sequentially with hexane to recover the SN1 fraction and DCM to elute the SN2 fraction. In the case of the alkanes fraction, the SN1 fraction contained the cleaned alkanes, and for the FAMEs, the SN2 fraction contained the cleaned FAMEs.

2.3. *n*-Alkane hydrogen isotopic analyses

For Bear Lake core sediments, the *n*-alkane stable hydrogen isotopic compositions were measured using a Thermo Scientific TRACE 1310 GC (30 m x 0.25 mm column, 0.25 μm coating, TG-5ms) connected to a Thermo Scientific Delta V Plus isotope ratio mass spectrometer (IRMS) with a Triplus RSH Sampler, a Conflo IV, and GC Isolink II at the University of

Arizona. The H_3^+ factor was monitored daily and averaged 2.9 ppm/nÅ (1σ = 0.1 ppm/nÅ) over a range of 1-8 V. Each sample run was bracketed with H_2 reference peaks, two of which were used for standardization. An external standard containing a mixture of 15 *n*-alkanes (C_{16} to C_{30}) with δD values ranging from -9‰ to -259‰ (A7 mix supplied by A. Schimmelmann, Indiana University, USA) was used to monitor and correct for machine drift.

For all other samples, *n*-alkane stable hydrogen isotopic compositions were analyzed using a Thermo Scientific TRACE 1610 GC (30 m x 0.25 mm column, 0.25 μm coating Rxi®-5ms) connected to a Thermo Scientific Delta Q IRMS with a Triplus RSH Smart Autosampler, a Conflo IV, and a GC Isolink II at the University of Southern California. H_3^+ was monitored daily and averaged 4.3 ppm/nÅ (1σ = 0.4 ppm/nÅ) over a range of 1-8 V. Each sample run was bracketed with H_2 reference peaks, two of which were used for normalization between standard and sample runs. All δD values were normalized to the international reference standard Vienna Standard Mean Ocean Water (VSMOW) using an external standard. The external standard contains a mixture of 15 *n*-alkanes (C_{16} to C_{30}) with δD values ranging from -17‰ to -256‰ (A6 mix supplied by A. Schimmelmann, Indiana University, USA). The RMS uncertainty (accuracy and precision) for δD was 4.8‰ (1σ = 1.6‰). Measurements were replicated at least twice with instrument precision of 2.0‰ (1σ = 1.9‰).

To convert the measured plant wax δD signal for the C_{31} *n*-alkane into δD_{precip}, we applied a constant fractionation factor $\varepsilon_{wax/water}$ = -94‰ ± 21‰ based on modern surveys of plant wax and plant water in the region (Feakins and Sessions, 2010). Feakins and Sessions (2010) found the site average $\varepsilon_{wax/water}$ had limited sensitivity to climate across the humidity gradient in modern-day southern California from forested coastal mountains to interior desert. Given this observation, the same constant $\varepsilon_{wax/water}$ value was used in a previous regional δD_{precip} reconstruction also based on the C_{31} *n*-alkane (Peaple et al., 2022) and we use this same value for consistency in these interpretations and comparability. We believe this assumption is reasonable as the plant taxa are similar, although the extent varies. Constraints on past fractionations are complicated to assess, but during glacial intervals, a descent in biomes may increase the extent of coniferous forests. However, as North American conifers produce minimal *n*-alkanes (Diefendorf et al., 2011), we do not expect the change in conifer proportions to affect our *n*-alkane δD_{precip} reconstructions. While we do not expect $\varepsilon_{wax/water}$ to vary substantially in this setting with

changes in the vegetation community on glacial-interglacial timescales, we acknowledge fractionation is always one of the largest unconstrained uncertainties on plant wax proxy reconstructions of δD_{precip}. To futher assess local fractionations we sampled modern plants and analyzed their isotopic composition (**Text S1-4**). To assess the potential size of fractionation changes associated with plant community changes, pollen-based apparent fractionation adjustments can be used (Feakins, 2013). Pollen reconstructions are available for Bear Lake and Great Salt Lake, but the the latter's record is low resolution and the dataset was not published (Davis, 1998). For Bear Lake, vegetation was composed entirely of C_3 vegetation, and grasses made up a minor component across glacial-interglacial cycles, making it unlikely for changes in vegetation composition to significantly influence $\varepsilon_{wax/water}$. We present pollen reconstructions alongside the constant fractionation δD_{precip} reconstructions to assess possible influences.

2.4. Comparisons to speleothem $\delta^{18}O$

To understand regional precipitation isotopic signals, we compared lacustrine leaf wax δD_{precip} to cave carbonate $\delta^{18}O$. We convert carbonate $\delta^{18}O$ (‰ VPDB) to drip water $\delta^{18}O$ (‰ VSMOW) by accounting for temperature-dependent fractionation of carbonate precipitation (Wackerbarth et al., 2010):

$$\delta^{18}O_{dripwater} = \frac{1.03086\left(\delta^{18}O_{calcite}+1000\right)}{e^{\frac{2780}{(T+273.15)^2}-0.00289}} - 1000 \quad (1)$$

where T is the temperature in °C of the cave site at the time of carbonate precipitation. The temperature used for each cave site was based on isotope-enabled Community Earth System Model Version 1.3 (iCESM1.3) output for the pre-industrial (for Holocene calculations) and for the LGM. For the Leviathan composite site, the simulated LGM-pre-industrial temperature difference was about 10°C (Zhu et al., 2017). For Devils Hole, cave temperatures were constant at 33.7°C due to hydrothermal influence and not thought to be responsive to air temperatures (Kluge et al., 2014). Thus, we did not apply a temperature-dependent fractionation correction to this site.

$\delta^{18}O_{dripwater}$ for both the Holocene and LGM were calculated using the averaged Holocene and LGM $\delta^{18}O_{calcite}$ values. The resulting $\delta^{18}O_{dripwater}$ values were then converted to $\delta D_{dripwater}$ based on the Global Meteoric Water Line:

$$\delta D = 8 \times \delta^{18}O + 10 \quad (2)$$

We assume $\delta D_{dripwater}$ reflects δD_{precip}, and compare the calculated $\delta D_{dripwater}$ from all cave sites to the calculated δD_{precip} from lacustrine plant wax records. However, we note that groundwater, cave dripwater, and plant water uptake all tend to be biased to winter recharge both based on the winter-dominance of precipitation in this region and the tendency of summer precipitation to evaporate rather than infiltrate (Friedman et al., 2002b).

3. Results and Discussion

3.1. Plant-based records of glacial-interglacial climate cycles

We found a large glacial-interglacial signal in calculated δD_{precip} at Great Salt Lake (**Figure 3b**) and Bear Lake (**Figure 3c**) with high values during interglacials and low values during glacials, correlating well with global atmospheric CO_2 and benthic foraminiferal $\delta^{18}O$ (Ahn et al., 2017; Bereiter et al., 2015). The δD_{precip} range at both Utah lake archives is similar in amplitude (~30‰) and absolute values (-155 to -125‰). We compare these two new 240-kyr records from Utah to a 200-kyr record from Searles Lake (CA) (Peaple et al., 2022), also based on C_{31} *n*-alkane-reconstructed δD_{precip} (**Figure 3d**). Though Great Salt Lake, Bear Lake, and Searles Lake all record broadly similar glacial-interglacial patterns of δD_{precip}, there are some differences in the detail and variability within the records that we do not attempt to pursue given differences in sampling resolution and age control. We note the deglacial δD_{precip} increase at Searles is larger at ~50‰ (**Figure 3d**) with greater D-enrichment at the Eemian interglacial (i.e., last interglacial), though the Holocene portion of the record is limited by the desiccation of this hypersaline, evaporative basin (Peaple et al., 2022). In contrast, at both Great Salt Lake and Bear Lake, absolute values for precipitation isotopes are lower (being further inland) and the amplitude of glacial-interglacial variability is smaller at ~30‰ (**Figure 3b-c**). Unlike Searles Lake, the Great Salt Lake record continues through the full Holocene as the saline water body persisted after a period of partial desiccation prior to the Holocene transition. Though these lakes have complex basin histories and are separated by 120 km (Great Salt Lake to Bear Lake) and 800 km (Great Salt Lake/Bear Lake to Searles Lake), all three record a consistent pattern of high δD_{precip} values during interglacials and low values during glacials, showing that this is a large-scale feature of the sub-continental scale hydroclimate in precipitation isotopic composition.

High δD_{precip} values also correspond to water stress as indicated by pollen records. Dry taxa pollen include *Amaranthaceae*, *Ambrosia*, and *Sarcobatus* at Great Salt Lake (Davis, 1977), *Ambrosia* and *Sarcobatus* at Bear Lake (Jimenez-Moreno et al., 2007), and *Amaranthaceae* and *Asteraceae* at Searles Lake (Peaple et al., 2022). At all three lakes, the greatest proportions of dry taxa occurred during D-enriched interglacials while the lowest proportions occurred during D-depleted glacials, indicating transitions between glacial pluvials and interglacial aridity with a classic 'saw-tooth' shaped pattern to each of the pollen records, although there are some differences in the variability and resolution of the records beyond those broad trends (**Figure 3b-d**). In addition to comparisons of wet-dry taxa, the pollen record can also be used to assess the probability of fractionation changes affecting plant wax δD as the plant community shifts (e.g., changes in grass proportions) (Feakins, 2013). We explored this using the high-resolution Bear Lake downcore pollen record and modern plant wax δD measurements, and found that allowing $\varepsilon_{wax/water}$ to vary according to shifting pollen compositions would not influence the observed glacial-interglacial trends in the C_{31} alkane-reconstructed δD_{precip} (**Text S10**).

Like shifting vegetation compositions, shifting climate states may also affect the apparent fractionation. Increased dry taxa during interglacials (decreased during glacials) may correspond to increased (decreased) evapotranspiration and decreased (increased) fractionation. While the modern interglacial fractionation value was regionally determined across a humidity gradient (Feakins and Sessions, 2010), it may need adjustment during the wetter conditions of glacial pluvials, with increased apparent fractionation and a corresponding upward correction in the calculated δD_{precip} which could act to reduce the magnitude of the glacial-interglacial variability, but this would then conflict with regional cave records (see section 3.2).

Across both new δD_{precip} records in this study from lakes in Utah, the Late Holocene values are broadly consistent with modern expectations. Late Holocene δD_{precip} averaged -126‰ (1σ = 5‰; n = 2) for Great Salt Lake and -131‰ (1σ = 2‰; n = 6) for Bear Lake. These averages are similar to modern Bear Lake catchment stream water δD of -123‰ (1σ = 9‰) (Custado et al., 2025), and Nov-Apr δD_{precip} values of -120‰ (1σ = 31‰) reported at Salt Lake City (Waterisotopes Database, 2024). Coherent signals in both lakes over the two glacial cycles imply a common precipitation isotopic composition or a common wax sourcing most likely achieved by regional aeolian transport of plant wax inputs into both lakes (Nelson et al., 2017). Fluvial

inputs would be unlikely to explain similar signals as the two lake basins and their fluvial catchments differ greatly today, and fluvial connectivity changed markedly across each lakes glacial-interglacial history (Kaufman et al., 2009; Oviatt et al., 1999). However, while Bear Lake δD_{precip} quickly dropped to ~ -135‰ after recording maximum values of ~ -120‰ early in the Holocene and Eemian, Great Salt Lake δD_{precip} remained consistent throughout the interglacial, suggesting differences in local inputs during interglacials. Perhaps background aeolian signals remained constant at Great Salt Lake while changes in river connectivity and basin closure led to inflow changes at Bear Lake as primary inflows switched between the Bear River during the glacial maxima and local streams during the interglacials when the Bear River was disconnected (Kaufman et al., 2009). Comparison to prior work by Peaple et al., (2022) on Searles Lake further south finds Searles Lake δD_{precip} also reached peak values of ~85‰ early in the Eemian but remained high only briefly (~4 kyr) before steadily dropping to ~100‰ by the end of the Eemian.

Both Utah lakes showed an increase in δD_{precip} of ~30‰ during the last two glacial terminations, T1 and T2. Comparing the two glacial intervals, the last glacial was 10‰ more D-enriched at Great Salt Lake and 4‰ more D-enriched at Bear Lake compared to the penultimate glacial (**Figure 3b,c**). This may be related to the nature of the forcing as the penultimate glacial (MIS 6) pCO_2 values drop at the beginning of the glacial, whereas they lower more gradually in the last glacial (MIS 5d-2; **Figure 3a**). At both lakes, millennial scale variability within glacials was ~20‰ (two-thirds the deglacial transition), but sampling resolution (~4 ky at Great Salt Lake, ~2 ky at Bear Lake) and age model uncertainty (up to 4 ky at Great Salt Lake, up to 7 ky at Bear Lake; **Figure S3, S4**) preclude detailed investigations of these features. Searles Lake had uniformly higher δD_{precip} (up to ~40‰) than the two Utah lakes (Peaple et al., 2022), reflecting less distillation due to reduced distance from the coast and potentially more evaporation during raindrop descent in the lowland setting, particularly in a drier interglacial atmosphere. Searles Lake showed a steady ~20‰ decrease in δD_{precip} over both glacial intervals and reached its lowest value during the penultimate glacial maximum. We also note both terminations have nearly two times larger glacial-interglacial amplitude at Searles Lake, potentially capturing greater details in variability compared to the Utah lakes.

The largest discrepancy between the two Utah lakes occurs during the penultimate interglacial, MIS 7 (~192–245 ka), a time period not recovered at Searles Lake further south. Globally, peak interglacial conditions occurred during MIS 7e (~245–234 ka) a time period not fully recovered at either Utah lake, followed by a brief return to glacial-like conditions in MIS 7d (~234–220 ka), and continuation of interglacial conditions from MIS 7c to 7a (~220–192 ka). Great Salt Lake recorded D-enriched signals during MIS 7c-a, but δD_{precip} values were 5–10‰ lower than the two later interglacials (**Figure 3b**). Bear Lake δD_{precip} values during MIS 7c-a were in the range of the succeeding glacial interval with no apparent D-enrichment (**Figure 3c**). Updated age models for both lakes indicate both cores recovered a complete history through MIS 7d, and likely terminate at the base of 7d or within MIS 7e, and thus may miss the peak interglacial conditions of MIS 7e as the cores end at 236.3 ± 6.7 ka for Great Salt Lake and 238.4±11.7 ka for Bear Lake (2σ age uncertainties; **Figures S2**, **S3**), thus we do not believe dating error to be the cause of the discrepancy. Further, Bear Lake pollen records (**Figure 3c**) show interglacial warming/drying during MIS 7d-a, with peak warm/arid taxa at the end of 7a (Jimenez-Moreno et al., 2007), so this is most likely a divergence in the proxies, with pollen and plant wax δD values responding differently across MIS 7. The plant wax record is also notably lower resolution compared to pollen which complicates the comparison. It is difficult to reconcile the lack of change in δD_{precip} across MIS 7d-a as precipitation should respond more readily to a changing climate than plant communities, but this may imply different windsheds for the two proxies along with local glacier/snow retreat being insufficient to register an "interglacial'" response in the plant waxes at this higher elevation lake, whereas it is seen at GSL. Although there are fewer terrestrial climate records for the penultimate interglacial, MIS 7 was indeed a weaker interglacial (i.e., colder) than the Holocene and Eemian, with ~30 ppm lower atmospheric pCO_2 (Bereiter et al., 2015) and ~0.3‰ higher benthic foraminiferal $\delta^{18}O$ (Ahn et al., 2017).

3.2. Lake and cave comparisons

We further compare the lacustrine plant wax δD_{precip} records (**Figure 4a**) with speleothem calcite $\delta^{18}O$ from several caves across the southwestern U.S. (**Figure 4b**). A composite timeseries obtained from Leviathan, Lehman, and Pinnacle Caves (NV) by Lachniet (2016) found a deglacial ^{18}O-enrichment of 5‰ at T1 and 3‰ at T2, though the two terminations were recorded at Leviathan and Lehman Caves respectively (**Figure 4b**). Interestingly, a larger ^{18}O-enrichment

(5‰) was recorded at 110 ka, exceeding that of the preceding T2, a feature not seen at any other site featured here (**Figure 4**). Speleothem calcite from Devils Hole (NV) shows a deglacial ^{18}O-enrichment of only 2‰ (**Figure 4b**), much lower than the Leviathan composite and likely due to Devils Hole's large aquifer integration (Winograd and Thordarson, 1975). Though at a lower resolution, select Devils Hole speleothems extended into MIS 7 and revealed a lower deglacial ^{18}O-enrichment of 1‰ compared to the later interglacials.

After conversion into δD_{precip} equivalency (see section 2.4), the Leviathan composite glacial-interglacial variability was ~30–50‰, similar to the three lake sites, while the continuous portion of the Devils Hole record was ~10–20‰, less than the lake sites. During MIS 7 at Devils Hole, the ^{18}O-enrichment was about half that of the Eemian, which would be ~10‰ in δD. This minimal ^{18}O-enriched at Devils Hole in MIS 7 is similar to the Great Salt Lake D-enrichment in MIS 7, suggesting this attenuated signal during the penultimate interglacial is a regional phenomenon.

We evaluate agreement between reconstructions of precipitation isotopes using correlation methods that account for serial correlation (Ebisuzaki, 1997) (**Figure S18**). Correlation analyses indicate the highest R values were obtained when comparing regional records using the same plant wax δD proxy at Great Salt Lake and Searles Lake ($R = 0.66$, $p << 0.05$), along with comparing both lakes to Devils Hole $\delta^{18}O$ ($R = 0.71$, $p << 0.05$ and $R = 0.80$, $p << 0.05$ respectively; Moseley et al., 2016). Though weaker, correlations were also found between plant wax records at Bear Lake and the more distal Searles Lake ($R = 0.58$, $p << 0.05$) and between Bear Lake and Devils Hole ($R = 0.49$, $p < 0.05$). The Leviathan record is uniquely variable, containing high and low frequencies, and thus, all comparisons to Leviathan $\delta^{18}O$ had $R < 0.35$ and had $p > 0.05$. Higher R values between the three lakes and Devils Hole likely stem from the prominent glacial-interglacial pattern in their isotopic values, in contrast to the Leviathan composite where orbital variability is more prominent. Lachniet (2016) attributed this to the speleothems' locations in the unsaturated zone, thus having fast response times to climatically driven changes in $\delta^{18}O$ of infiltrating water. Leviathan is also notable in having not only a prominent Eemian peak, but a secondary peak with greater ^{18}O-enrichment at 100 ka not seen in other records. The 100-ka peak in $\delta^{18}O$ was preceded by an extreme low at 110 ka which Lachniet (2016) attributed to a cold, high latitude moisture source that coincided with a

prominent minimum in northern hemisphere summer insolation. This 110 ka $\delta^{18}O$ drop was 2‰ lower than during the penultimate glacial maximum, a feature unique to the Leviathan composite and likely not reflective of regional precipitation isotope trends. We also note that the Leviathan composite switches from Lehman to Leviathan Cave at 105 ka, and spatial adjustments in precipitation $\delta^{18}O$ between the two caves may have contributed to the magnitude of ^{18}O-enrichment for the 110-100 ka feature. While lake records have lower resolutions, each should be sufficient to register the 110-100-ka transition if present regionally, as should Devils Hole.

In addition to the long records introduced previously, shorter-duration lake and cave proxy archives distributed across the southwestern U.S. similarly show a deglacial enrichment in the heavier isotope during T1 (Asmerom et al., 2010; Feakins et al., 2019; Wagner et al., 2010). The largest offset is seen at the site nearest to the coast–an *n*-alkanoic acid δD_{precip} record from Lake Elsinore (CA) showing a ~60‰ deglacial D-enrichment (Feakins et al., 2019). We note that it is possible the magnitude of D-enrichment may have been amplified by aquatic production of *n*-alkanoic acids from D-enriched lake waters in the Holocene. Farther inland to the south, Cave of the Bells (AZ) and Fort Stanton Cave (NM) both had calculated δD increases of ~30‰ during T1, although both sites are notably in a different climatic regime strongly influenced by the summer monsoon (Asmerom et al., 2010; Wagner et al., 2010). While all previous lake and cave sites lie on a southwest-northeast trending transect across the Great Basin, Cave of the Bells and Fort Stanton Cave lie over 800 km southeast of this transect and receive some summer precipitation from the North American Monsoon. Regardless, the amplitude of glacial-interglacial offset at these sites is remarkably consistent with sites in the transect. One regional record that is an exception is an alpine fen *n*-alkane δD_{precip} record from Cumbres Bog (CO), which showed D-depletion rather than D-enrichment from the LGM to the Holocene (Todd et al., 2025). This divergent record may be influenced by local environmental change, such as drying or vegetation assemblage shifts, that confounded regional precipitation isotopic signals, or it may represent a different climate signal altogether as the site is located much further in the continental interior compared to all previous sites. Despite slight differences in signal amplitudes and timing, all but one record share the same sign of change between glacials and interglacials (**Figure 5**). In the next sections, we discuss the possible thermodynamic and atmospheric circulation mechanisms that drive this pattern.

3.3. Drivers of glacial-interglacial cycles in precipitation isotopes

The 30‰ glacial D-depletion at the two new records from Utah is coherent with regional patterns in precipitation isotopic values (**Figure 5**). Several mechanisms can contribute to this D-depletion including lower condensation temperatures, a greater proportion of precipitation falling as snow rather than rain, increased sourcing of moisture from higher latitudes, and/or a change in prior rainout (Dansgaard, 1964). Here, we consider each mechanism and quantify their likely contributions.

The precipitation isotope response to temperature has been widely documented and may play a large role in glacial-interglacial precipitation isotopic signals (**Mechanism 1**). In Salt Lake City, monthly δD_{precip} increases with temperature at a rate of 4‰/°C (Global Network of Isotopes in Precipitation, 2022), similar to initial observations by Dansgaard (1964) in the North Atlantic (**Figure S19**). Paleothermometry of the Bonneville Basin based on amino acids has suggested a cooling of 5.5±3.1°C in MIS 2 relative to the Early Holocene (Kaufman, 2003) while plant macrofossil assemblages relative to modern communities suggest a median LGM cooling of ~6°C (Harbert and Nixon, 2018). Modeled air temperatures suggest a glacial cooling of 8°–10°C per Quirk et al. (2018), 7.5±2.6°C per Oster et al. (2015), and ~11°C per iCESM1.3 simulations (Zhu et al., 2017) relative to pre-industrial (PI). A cooling of 5°–11°C equates to a 20–44‰ decrease in δD_{precip} based on the modern temperature/δD slope. Temperature is thus capable of explaining over half to all of the ~30‰ glacial D-depletion at Great Salt Lake and Bear Lake. As cooling greater than 7.5°C would result in a D-depletion greater than 30‰, we expect glacial cooling to be within the lower range of previous estimates.

In addition, cooler temperatures would likely lead to an increase in the proportion of precipitation falling as snow, which would further lower δD_{precip} (**Mechanism 2**). Presently, 20%–30% of the annual liquid precipitation is from snow (as SWE) at the two lake sites (National Centers for Environmental Information, 2020a, b). Annual δD_{precip} is estimated to be -103‰ ± 2‰ at Great Salt Lake and -112‰ ± 1‰ at Bear Lake (Waterisotopes Database, 2025a, b). Snow pit measurements from the Wasatch Range have a δD of -148 ± 15‰ (Waterisotopes Database, 2017a, b, c, d). Using a linear mixing model, we calculate the proportional increase in SWE needed to account for lower δD_{precip} not due to cooling temperatures (**Text S11**). For a

minimum cooling of 5°C, Great Salt Lake and Bear Lake require SWE to increase by 17.8% and 19.4% respectively to yield a D-depletion of 10‰, placing an upper bound on the role of snowfall and allowing temperature and snowfall together to completely explain the observed signal. In the southwestern US, winter precipitation dominates groundwater recharge (Friedman et al., 2002b) and also supplies water to the major rivers and streams entering Great Salt Lake and Bear Lake. As changes in temperature and snow proportion are sufficient to explain the ~30‰ glacial D-depletion, this strongly suggests the glacial-interglacial precipitation isotope records are dominated by large-scale thermodynamics. Our suggestion of a dominant temperature-dependent isotope effect is consistent with non-isotope enabled Coupled Model Intercomparison Project phase 5/Paleoclimate Modeling Intercomparison Project phase 3 (CMIP5/PMIP3) experiments by Morrill et al. (2018) who found thermodynamics explained a greater portion of the glacial pluvial in climate model experiments than did storm track changes, with increased moisture advection primarily due to the greater land-sea temperature contrast. A similar conclusion about the importance of thermodynamics (both decreased evaporation and increased precipitation) was reached for a recent analysis of Lake Bonneville water balance and climate model comparisons (Mering et al., 2026).

Nevertheless, storm track changes are expected given the presence of the Laurentide ice sheet (**Mechanism 3**). With combined effects from thermodynamics and topographic steering, most climate model simulations suggest increased winter season rainfall during glacial maximum and deglacial pluvials. Proposed mechanisms include shifts in the latitudinal position, trajectory, and/or strength of the midlatitude jet (Fu, 2023; Lora et al., 2016; Oster et al., 2015; Wong et al., 2016). Although some modeling studies linked moisture increase to increases in the quantity, intensity, or penetration of southwesterly atmospheric rivers, particularly in the deglacial (Lora et al., 2017; McGee et al., 2018; Oster et al., 2023), another study found that despite greater overall westerly moisture delivery, atmospheric river activity was reduced during the LGM (Lora et al., 2023). While the ~30‰ glacial D-depletion can be explained by thermodynamics alone, we can consider how changes in storm tracks may contribute to this D-depletion. Measured values for modern precipitation at Cedar City (UT) found high latitude, North Pacific moisture sources have a δD_{precip} of -112±37‰ while low latitude, tropical Pacific sources have values of -81 ± 37‰ (Friedman et al., 2002a). A 32.4% proportional increase in North Pacific storms is needed to produce a 10‰ decrease in δD_{precip} under minimum cooling estimates of 5°C, with this

526 percentage decreasing for a greater degree of cooling (**Text S12**). We note that storm trajectories
527 measured at Cedar City would have experienced less prior rainout, leading to higher overall
528 δD_{precip} values than at Great Salt Lake and Bear Lake in our study which are further inland.

529 Two southwestern U.S. cave records are located in the summer North American Monsoon
530 (NAM)-influenced zone: Cave of the Bells (AZ) and Fort Stanton Cave (NM). Wagner et al.
531 (2010) and Asmerom et al. (2010) attributed the caves' LGM ^{18}O-depletion to an increase in
532 winter season Pacific storms and a weakening influence of NAM during colder glacials. This is
533 consistent with D-depletion in the Gulf of California plant wax δD record of Bhattacharya et al.
534 (2018), as entrainment of dry, cold air during a colder climate weakens summer rainfall
535 (Bhattacharya et al., 2017). Though a glacial reduction in summer rainfall is likely, we highlight
536 here how the influence of cooling alone on winter season precipitation can explain similar
537 magnitudes of change in the region.

538 Changes in the proportional distillation associated with rainout can also cause changes in
539 precipitation isotopic composition as an air mass moves inland (**Mechanism 4**). A colder glacial
540 climate with a steeper land-sea temperature gradient is modelled to yield a greater moisture
541 advection (Morrill et al., 2018), greater rainout efficiency and D-depletion (Kukla et al., 2019;
542 Tabor et al., 2021), but under pluvial conditions, this may be partially countered by increased
543 moisture recycling with greater evapotranspiration in a more vegetated landscape (Kukla et al.,
544 2019; Mering et al., 2026; Winnick et al., 2014). Thus, we may see an attenuated continental
545 effect during glacial climates compared to the Holocene.

546 ### 3.4. Proxy-model comparison

547 To further explore mechanisms, we compare the assembled proxy records with isotope-enabled
548 climate model outputs using iCESM1.3 (Zhu et al., 2017). We first evaluate model performance
549 in capturing PI and LGM conditions. At Great Salt Lake and Bear Lake, we find PI simulated
550 temperatures generally matched well with modern measurements in both absolute values and
551 seasonal patterns (**Figure S21a,b**). PI simulated precipitation amount had similar absolute
552 values, but not seasonal patterns as precipitation peaked in late spring rather than winter, causing
553 spring precipitation to be up to 60 mm higher than modern (**Figure S21c,d**). PI simulated
554 monthly δD_{precip} had a similar annual average to modern measurements (-110‰ to -100‰), but a

much lower seasonal amplitude (~30‰) than modern (~100 ‰) (**Figure S21e,f**). Looking at the whole southwestern U.S., we find LGM simulated precipitation was higher than PI only along the coast, but drier for the majority of the Great Basin including at the two Utah lakes in conflict with observations (**Figure S22c**). The model experiments did not successfully simulate the LGM pluvial established by numerous proxy records. Clear geomorphological evidence for the presence of expanded LGM pluvial lakes, including Searles Lake, Lake Bonneville, and Lake Lahontan, imply wetter conditions, and by their evaporative flux would have contributed moisture to the atmosphere inland (Mering et al., 2026). The lack of high-resolution topography, including absence of the Sierra Nevada, in the model may also have contributed to insufficient precipitation amounts as moisture moved inland (Mering et al., 2026). Future representation of pluvial lakes in the boundary conditions for LGM simulations along with more detailed topography may help to improve representation of the pluvial conditions and reduce the continental effect that presently dominates the inland isotopic gradient (**Figure 6b**).

Model simulations in their current formulation were also unable to capture an accurate spatial gradient in D-depletion. LGM simulated δD_{precip} sharply declines inland due to distillation, whereas the gradient in proxies is much flatter, presumably sustained by moisture recycling, a feedback absent in the too-dry model simulations that would be supplemented if large inland lakes were prescribed (**Figure 6b**). The modelled glacial-interglacial difference in δD_{precip} contrasts with that of the proxies as well (**Figure 6c**). Models predict the glacial-interglacial difference in δD_{precip} to increase in amplitude farther inland, because the model is dominated by increased Rayleigh distillation efficiency in a colder atmosphere (**Figure 6c**). Proxies, however, showed the largest glacial-interglacial offset nearer to the coast, including Lake Elsinore, Searles Lake, and the Leviathan composite, likely dominated by the temperature effect (**Mechanisms 1** and **2**), with the offset decreasing further inland, consistent with more moisture recycling in a pluvial climate.

In addition to iCESM1.3, we also considered its derivative the isotope-enabled Transient Climate Experiment (iTraCE) for the last deglacial (He et al., 2021; Zhu et al., 2017), and we examined the LGM data assimilation (lgmDA) (Tierney et al., 2020) and the LGM Reanalysis (LGMR) (Osman et al., 2021). Similar to iCESM1.3 simulations, all model and data assimilation products consistently had smaller LGM-PI δD offsets than proxy records at the same site, and these

offsets also generally increased when moving inland (**Figure 7**). Devils Hole is an exception due to its hydrothermal influence, which climate models and data assimilation products do not account for. As none of these models prescribe large pluvial lakes nor have detailed topography, the similarity in their simulated δD offsets can be expected. Therefore, we find these climate model experiments are currently unable to reliably inform mechanisms for precipitation isotopes in the glacial pluvial because they do not simulate a regionally expansive pluvial climate state. With the availability of proxy evidence from sites outside the Great Basin, it is possible the addition of large lakes to the model may not completely explain spatial patterns in proxy δD_{precip}, and may thus require the prescription of higher resolution topography in addition to pluvial lakes. All models and data assimilation products referenced here have a 2° resolution in the land and atmosphere. In the model, elevation steadily increases moving from the coast inland towards the Rocky Mountains, and key sub-grid scale topographic barriers and features in the southwestern US, including the Sierra Nevada and the Great Basin, are absent. The lack of blocking topography underestimates orographic rainout and inland rainshadow effects in the PI simulations and overestimates temperature and continental Rayleigh distillation effects in the LGM. In addition, the lack of large glacial pluvial lakes underestimates continental moisture recycling that would counteract the continental effect (Mering et al., 2026). Misrepresentation of rainfall amount and distribution will also lead to inaccurately simulated δD_{precip}. We hope that highlighting this LGM discrepancy, in the context of greater confidence from increased proxy data density can motivate efforts to improve representation of pluvial conditions, in particular by representing the known extent of paleolakes and more detailed topography in the boundary conditions, as well as to motivate time transient simulations for the penultimate glacial termination.

We acknowledge that for cave carbonates, our simplified conversion of carbonate $\delta^{18}O$ into drip water δD considering only temperature-dependent fractionation discounted other influencing factors such as water modification during soil infiltration, cave relative humidity, cave pCO_2, amongst others. Tabor et al. (2021) extended beyond the iCESM $\delta^{18}O_{precip}$ output by simulating speleothem $\delta^{18}O$ using proxy forward models to account for cave environmental factors. They reported greater agreement between their simulated and measured speleothem $\delta^{18}O$ compared to the proxy-model comparisons here, which suggests cave processes amplified the LGM-PI signal. However, here we show that amplitudes in cave carbonate $\delta^{18}O$, when converted into δD space

616 considering a factor of eight and air temperature effects (with the exclusion of Devils Hole which
617 is geothermally heated), are consistent with amplitudes in plant wax δD. Thus, rather than cave
618 processes amplifying the LGM-PI signal, it is the model that is suppressing this signal, causing
619 simulated LGM-PI offsets to be smaller than that of proxy archives. Proxy offsets show much
620 larger relative depletions in heavy isotopes across the region that is not simulated by models, and
621 we attribute this to inaccurately simulated pluvial rainfall amounts counteracting distillation
622 isotopic effects.

623 **4. Conclusions**

624 We reconstruct precipitation isotopes over the last two glacial cycles, using plant waxes archived
625 in Great Salt Lake and Bear Lake sediments, in Utah, USA. The dual lake record isolates
626 concerns about lake basin differences, complexity in age models, local plant types, catchment
627 connectivity, and limnological conditions. We find both lakes present a largely coherent record
628 of precipitation isotopes, suggesting coeval shifts in regional precipitation patterns and/or shared
629 aeolian sourcing of leaf waxes regardless of catchment differences. Climate signals appear
630 synchronous to the extent of dating confidence, with additional U-Th dates for Great Salt Lake
631 and an updated Bayesian age model for Bear Lake. In particular, these long-spanning records
632 permit a comparison of the last three interglacials, revealing MIS 7 to be considerably weaker
633 than the latter two. Our two new records, in combination with previously published regional lake
634 and cave archives, all show coherent trends in precipitation isotopes, a robust signal of a large-
635 scale regional hydroclimate state over the last glacial cycle and likely the last two cycles. Given
636 the large-scale regional coherency, thermodynamics alone could explain most, if not all, of the
637 glacial depletion in heavy isotopes in precipitation isotopes without invoking changes in
638 atmospheric dynamics. Comparison to climate model outputs and data assimilation products
639 reveal that, while models predict limited D-depletion, proxies yielded much larger amplitudes of
640 depletion, with model-proxy differences decreasing towards the continental interior. This
641 fundamental difference between proxies and models suggests further model refinement, such as
642 with prescription of large pluvial lakes during glacial maxima along with higher resolution
643 topography on the land surface, is needed for accurate precipitation isotope simulations. Our new
644 Utah lake records, resolving two pluvials at two glacial terminations, present additional proxy
645 information for model refinement of not only deglacial T1, but also the much less studied T2.

646 This addition of two precipitation isotopic reconstructions of T2, when such reconstructions are
647 already sparse, now place them as promising comparisons to a time transient T2 climate model
648 simulation.

649 **Acknowledgements**

650 This study was supported by the U.S. National Science Foundation Grant NSF-EAR-2152630
651 and NSF-P4Climate-2303418 to S.F., the Packard Fellowship for Science and Engineering to JT,
652 the Continental Scientific Drilling (CSD) Facility's visiting graduate student travel grant to R.S.,
653 the USC Wrigley Institute Graduate Fellowship to R.S., and the 2024 AGeS-Grad grant to R.S.
654 Sediment core material used in this project was provided by CSD. Fieldwork was supported by
655 the U.S. National Science Foundation Grant NSF-AGS- 2102901 to D.E.I. We thank Corey
656 Shaver for performing stable hydrogen isotopes analyses of Bear Lake samples. We thank USC
657 undergraduates Betelhem Assefa, Britney Vu, Sean Cheng, Vivian Wu, and Iris Shen for
658 laboratory assistance, Kristina Brady Shannon for assistance at the CSD core repository, and
659 Jonah Berstein-Schalet for help in the field. We thank Christopher Kinsley, Justin Custado,
660 Natalie Burls, Paul Acosta, and Allegra Legrande for helpful discussions, as well as the helpful
661 comments of Joseph Novak and another anonymous reviewer, the Associate Editor, and Editor
662 Matthew Huber.

663 **Supporting Information**

664 Supporting Information may be found in the online version of this article.

665 **Conflict of Interest**

666 The authors declare no financial conflicts of interest for any author or their affiliations.

667 **Open Research**

668 Data files are archived at the NOAA paleoclimatology database (So et al., 2025).

669 **Figure Captions**

670 **Figure 1**. Maps showing locations of a) Great Salt Lake and Bear Lake (yellow stars) alongside
671 western U.S. sites with paleoclimate records referenced (green dots) and mentioned (gray dots)

672 in this study and the Great Basin boundary (white), b) present-day extent of Great Salt Lake and
673 Bear Lake (dark blue) and their peak lake level extent during the Last Glacial Maximum to
674 deglacial (light blue), and c) the drill sites for the sediment cores used in this study at Great Salt
675 Lake (GLAD1-GSL00-4) and Bear Lake (GLAD1-BL00-1).

676 **Figure 2.** Monthly precipitation amounts (blue bars), temperatures (red lines), and precipitation
677 δD estimates (black lines) for a) Salt Lake City, UT (southeast of Great Salt Lake), and b)
678 Laketown, UT (south of Bear Lake). Precipitation amounts, with snow converted to snow water
679 equivalent (SWE), and temperatures are averaged for 1991–2020 (National Centers for
680 Environmental Information, 2020a, b). Precipitation δD is interpolated from the Waterisotopes
681 Database (2025a, 2025b).

682 **Figure 3.** Glacial-interglacial climate variability shown in a) atmospheric pCO_2 from the EPICA
683 Dome C ice core (green; Bereiter et al., 2015) and stacked benthic foraminiferal $\delta^{18}O$ (brown;
684 Ahn et al., 2017); and δD_{precip} from b) Great Salt Lake (gray; this study), c) Bear Lake (black;
685 this study), and d) Searles Lake (purple; Peaple et al., 2022). Pollen percentages for dry taxa are
686 shown for b) Great Salt Lake (Davis, 1998), c) Bear Lake (Jimenez-Moreno et al., 2007), and d)
687 Searles Lake (Peaple et al., 2022). Shading shows interglacials (pink), glacial terminations
688 (yellow), and glacial maxima (blue). Great Salt Lake experienced two intervals of partial
689 desiccation (salts) preceded by two intervals of lake highstand and areal expansion (Bonneville
690 and Little Valley, see Balch et al. (2005)). Searles Lake desiccated completely near the core top.

691 **Figure 4.** Comparison of precipitation isotope timeseries from a) Great Salt Lake (gray; this
692 study), Bear Lake (black; this study), and Searles Lake (purple; Peaple et al., 2022), with b)
693 speleothem calcite $\delta^{18}O$ from the Leviathan, Lehman, and Pinnacle Cave composite (blue;
694 Lachniet, 2016) and Devils Hole sampled at different depths within the cave (red; Wendt et al.,
695 2025). See **Figure 1a** for the locations of all sites.

696 **Figure 5.** Comparison of average glacial (blue) and interglacial (red) precipitation δD (for leaf
697 waxes) and drip water δD (for cave carbonate) in regional proxy records. Sites are ordered by
698 distance from the coast. Cave of the Bells and Fort Stanton, as they are in a different climate
699 regime strongly affected by the summer monsoon, are placed on a separate set of lines (see text).
700 Devils Hole and Cumbres Bog are also left off the line, the former due to its hydrothermal

701 influence and the latter due to different climate signal (see text). For sites with both the full T1
702 and T2, the left, large symbol is T1 and right, small symbol is T2. Error bars show 1σ of the δD
703 values averaged over that time period.

704 **Figure 6.** Comparison of proxy records (symbols) to iCESM1.3-modeled δD_{precip} (base map)
705 during a) the pre-industrial (PI) compared to proxies, averaged across their Holocene extent, b)
706 the Last Glacial Maximum (LGM), and c) the difference between the LGM and PI. Symbols
707 differentiate proxy types (triangle = *n*-alkane δD, square = *n*-alkanoic acid δD, circle = cave
708 carbonate $\delta^{18}O$) all presented as precipitation or drip water δD equivalent. For references to
709 individual proxy sites, see **Figure 5**.

710 **Figure 7.** Comparison of LGM-PI precipitation/drip water δD differences between proxy data
711 (black bars) and climate model outputs/data assimilation products (colored bars). Sites are
712 ordered by distance from the coast.

713 **References**

714 Ahn, S., Khider, D., Lisiecki, L.E. and Lawrence, C.E. (2017) A probabilistic Pliocene–
715 Pleistocene stack of benthic $\delta^{18}O$ using a profile hidden Markov model. Dynamics and Statistics
716 of the Climate System 2.10.1093/climsys/dzx002.

717 Asmerom, Y., Polyak, V.J. and Burns, S.J. (2010) Variable winter moisture in the southwestern
718 United States linked to rapid glacial climate shifts. Nature Geoscience 3, 114-
719 117.10.1038/ngeo754.

720 Balch, D.P., Cohen, A.S., Schnurrenberger, D.W., Haskell, B.J., Garces, B.L.V., Beck, J.W.,
721 Cheng, H. and Edwards, R.L. (2005) Ecosystem and paleohydrological response to Quaternary
722 climate change in the Bonneville Basin, Utah. Palaeogeography Palaeoclimatology
723 Palaeoecology 221, 99-122.10.1016/j.palaeo.2005.01.013.

724 Benson, L.V., Burdett, J.W., Kashgarian, M., Lund, S.P., Phillips, F.M. and Rye, R.O. (1996)
725 Climatic and Hydrologic Oscillations in the Owens Lake Basin and Adjacent Sierra Nevada,
726 California. Science 274, 746-749.10.1126/science.274.5288.746.

727 Bereiter, B., Eggleston, S., Schmitt, J., Nehrbass-Ahles, C., Stocker, T.F., Fischer, H., Kipfstuhl,
728 S. and Chappellaz, J. (2015) Revision of the EPICA Dome C CO_2 record from 800 to 600kyr
729 before present. Geophysical Research Letters 42, 542-549.10.1002/2014gl061957.

730 Bhattacharya, T., Tierney, J.E., Addison, J.A. and Murray, J.W. (2018) Ice-sheet modulation of
731 deglacial North American monsoon intensification. Nature Geoscience 11, 848-
732 +.10.1038/s41561-018-0220-7.

733 Bhattacharya, T., Tierney, J.E. and DiNezio, P. (2017) Glacial reduction of the North American
734 Monsoon via surface cooling and atmospheric ventilation. Geophysical Research Letters 44,
735 5113-5122.https://doi.org/10.1002/2017GL073632.

736 Blaauw, M. and Christen, J.A. (2011) Flexible Paleoclimate Age-Depth Models Using an
737 Autoregressive Gamma Process. Bayesian Analysis 6, 457-474.10.1214/ba/1339616472.

738 Bowen, G.J., Nielson, K.E. and Eglinton, T.I. (2019) Multi-substrate radiocarbon data constrain
739 detrital and reservoir effects in Holocene sediments of the Great Salt Lake, Utah. Radiocarbon
740 61, 905-926.10.1017/rdc.2019.62.

741 Broecker, W.S. and Kaufman, A. (1965) Radiocarbon Chronology of Lake Lahontan and Lake
742 Bonneville II, Great Basin. GSA Bulletin 76, 537-566.10.1130/0016-
743 7606(1965)76[537:RCOLLA]2.0.CO;2.

744 Colman, S.M., Kaufman, D.S., Bright, J., Heil, C., King, J.W., Dean, W.E., Rosenbaum, J.G.,
745 Forester, R.M., Bischoff, J.L., Perkins, M. and McGeehin, J.P. (2006) Age model for a
746 continuous, ca 250-ka Quaternary lacustrine record from Bear Lake, Utah-Idaho. Quaternary
747 Science Reviews 25, 2271-2282.10.1016/j.quascirev.2005.10.015.

748 Custado, M.J., Gagnon, C.A., Belanger, B., Sekhon, N., Bernstein-Schalet, J., Kinsley, C.W.,
749 Sharp, W.D., Oster, J.L. and Ibarra, D.E. (2025) Constraining the Modern Hydrological Balance
750 of Bear Lake, Utah-Idaho: Insights From Stable Isotopes ($\delta^{18}O$ and $\delta^{2}H$). Water Resources
751 Research 61, e2024WR038264.https://doi.org/10.1029/2024WR038264.

752 Dansgaard, W. (1964) Stable isotopes in precipitation. Tellus 16, 436-
753 468.https://doi.org/10.1111/j.2153-3490.1964.tb00181.x.

754 Davis, A.M. (1977) The Prairie-Deciduous Forest Ecotone in the Upper Middle West. Annals of
755 the Association of American Geographers 67, 204-213.https://doi.org/10.1111/j.1467-
756 8306.1977.tb01133.x.

757 Davis, J., Gwynn, J.W. and Rupke, A. (2022) Commonly Asked Questions About Utah's Great
758 Salt Lake and Ancient Lake Bonneville, in: Utah Department of Natural Resources (Ed.), 2nd ed.
759 Utah Geological Survey, Salt Lake City, UT

760 Davis, O.K. (1998) Palynological evidence for vegetation cycles in a 1.5 million year pollen
761 record from the Great Salt Lake, Utah, USA. Palaeogeography, Palaeoclimatology,
762 Palaeoecology 138, 175-185.https://doi.org/10.1016/S0031-0182(97)00105-3.

763 Diefendorf, A.F., Freeman, K.H., Wing, S.L. and Graham, H.V. (2011) Production of n-alkyl
764 lipids in living plants and implications for the geologic past. Geochimica Et Cosmochimica Acta
765 75, 7472-7485.10.1016/j.gca.2011.09.028.

766 Ebisuzaki, W. (1997) A Method to Estimate the Statistical Significance of a Correlation When
767 the Data Are Serially Correlated. Journal of Climate 10, 2147-2153.https://doi.org/10.1175/1520-
768 0442(1997)010<2147:AMTETS>2.0.CO;2.

769 Feakins, S.J. (2013) Pollen-corrected leaf wax D/H reconstructions of northeast African
770 hydrological changes during the late Miocene. Palaeogeography, Palaeoclimatology,
771 Palaeoecology 374, 62-71.https://doi.org/10.1016/j.palaeo.2013.01.004.

772 Feakins, S.J. and Sessions, A.L. (2010) Controls on the D/H ratios of plant leaf waxes in an arid
773 ecosystem. Geochimica Et Cosmochimica Acta 74, 2128-2141.10.1016/j.gca.2010.01.016.

774 Feakins, S.J., Wu, M.S., Ponton, C. and Tierney, J.E. (2019) Biomarkers reveal abrupt switches
775 in hydroclimate during the last glacial in southern California. Earth and Planetary Science Letters
776 515, 164-172.10.1016/j.epsl.2019.03.024.

777 Friedman, I., Harris, J.M., Smith, G.I. and Johnson, C.A. (2002a) Stable isotope composition of
778 waters in the Great Basin, United States 1. Air-mass trajectories. Journal of Geophysical
779 Research: Atmospheres 107, ACL 14-11-ACL 14-14.https://doi.org/10.1029/2001JD000565.

780 Friedman, I., Smith, G.I., Johnson, C.A. and Moscati, R.J. (2002b) Stable isotope compositions
781 of waters in the Great Basin, United States 2. Modern precipitation. Journal of Geophysical
782 Research: Atmospheres 107, ACL 15-11-ACL 15-22.https://doi.org/10.1029/2001JD000566.

783 Fu, M. (2023) Revisiting Western United States Hydroclimate During the Last Deglaciation.
784 Geophysical Research Letters 50, e2022GL101997.https://doi.org/10.1029/2022GL101997.

785 Global Network of Isotopes in Precipitation (2022) Salt Lake City (Utah), International Atomic
786 Energy Agency

787 Harbert, R.S. and Nixon, K.C. (2018) Quantitative Late Quaternary Climate Reconstruction from
788 Plant Macrofossil Communities in Western North America. Open Quaternary.10.5334/oq.46.

789 He, C., Liu, Z., Otto-Bliesner, B.L., Brady, E.C., Zhu, C., Tomas, R., Clark, P.U., Zhu, J., Jahn,
790 A., Gu, S., Zhang, J., Nusbaumer, J., Noone, D., Cheng, H., Wang, Y., Yan, M. and Bao, Y.
791 (2021) Hydroclimate footprint of pan-Asian monsoon water isotope during the last deglaciation.
792 Science Advances 7, eabe2611.doi:10.1126/sciadv.abe2611.

793 Jackson, S.T., Betancourt, J.L., Lyford, M.E., Gray, S.T. and Rylander, K.A. (2005) A 40,000-
794 year woodrat-midden record of vegetational and biogeographical dynamics in north-eastern
795 Utah, USA. Journal of Biogeography 32, 1085-1106.10.1111/j.1365-2699.2005.01251.x.

796 Jimenez-Moreno, G., Anderson, R.S. and Fawcett, P.J. (2007) Orbital- and millennial-scale
797 vegetation and climate changes of the past 225 ka from Bear Lake, Utah-Idaho (USA).
798 Quaternary Science Reviews 26, 1713-1724.10.1016/j.quascirev.2007.05.001.

799 Kaufman, D.S. (2003) Amino acid paleothermometry of Quaternary ostracodes from the
800 Bonneville Basin, Utah. Quaternary Science Reviews 22, 899-
801 914.https://doi.org/10.1016/S0277-3791(03)00006-4.

802 Kaufman, D.S., Bright, J., Dean, W.E., Rosenbaum, J.G., Moser, K., Anderson, R.S., Colman,
803 S.M., Heil, C.W., Jimenez-Moreno, G., Reheis, M.C. and Simmons, K.R. (2009) A quarter-
804 million years of paleoenvironmental change at Bear Lake, Utah and Idaho, Paleoenvironments of
805 Bear Lake, Utah and Idaho, and Its Catchment. Geological Soc Amer Inc, Boulder, pp. 311-351.

806 Kelts, K., Cohen, A., Davis, O., Dean, W., Dinter, D., Nielson, D., Oviatt, C.G., Rosenbaum, J.,
807 Haskell, B., Honke, J., King, J.C., Kruger, N., Palacios-Fest, M., Schnurrenberger, D., Skipp, G.,
808 Valero-Garcés, B.L., Anderson, S., Bright, J., Heil, C., Kaufman, D. and Moser, K. (2000) Initial
809 Reports of the Global Lakes Drilling Program, in: Schnurrenberger, D., Haskell, B. (Eds.).
810 University of Arizona; Limnological Research Center, University of Minnesota; Northern
811 Arizona University; University of Utah; United States Geological Survey; University of Rhode
812 Island, Graduate School of Oceanography

813 Kirby, M.E., Feakins, S.J., Bonuso, N., Fantozzi, J.M. and Hiner, C.A. (2013) Latest Pleistocene
814 to Holocene hydroclimates from Lake Elsinore, California. Quaternary Science Reviews 76, 1-
815 15.https://doi.org/10.1016/j.quascirev.2013.05.023.

816 Kluge, T., Affek, H.P., Dublyansky, Y. and Spötl, C. (2014) Devils Hole paleotemperatures and
817 implications for oxygen isotope equilibrium fractionation. Earth and Planetary Science Letters
818 400, 251-260.https://doi.org/10.1016/j.epsl.2014.05.047.

819 Kukla, T., Winnick, M.J., Maher, K., Ibarra, D.E. and Chamberlain, C.P. (2019) The Sensitivity
820 of Terrestrial $\delta^{18}O$ Gradients to Hydroclimate Evolution. Journal of Geophysical Research:
821 Atmospheres 124, 563-582.https://doi.org/10.1029/2018JD029571.

822 Laabs, B.J.C. and Kaufman, D.S. (2003) Quaternary highstands in Bear Lake Valley, Utah and
823 Idaho. GSA Bulletin 115, 463-478.10.1130/0016-7606(2003)115<0463:Qhiblv>2.0.Co;2.

824 Lachniet, M. (2016) A Speleothem Record of Great Basin Paleoclimate: The Leviathan
825 Chronology, Nevada, Lake Bonneville: A Scientific Update. Elsevier Science BV, Sara
826 Burgerhartstraat 25, PO box 211, 1000 AE Amsterdam, Netherlands, pp. 551-569.10.1016/b978-
827 0-444-63590-7.00020-2.

828 Lachniet, M.S., Denniston, R.F., Asmerom, Y. and Polyak, V.J. (2014) Orbital control of
829 western North America atmospheric circulation and climate over two glacial cycles. Nature
830 Communications 5, 3805.10.1038/ncomms4805.

831 Lora, J.M., Mitchell, J.L., Risi, C. and Tripati, A.E. (2017) North Pacific atmospheric rivers and
832 their influence on western North America at the Last Glacial Maximum. Geophysical Research
833 Letters 44, 1051-1059.https://doi.org/10.1002/2016GL071541.

834 Lora, J.M., Mitchell, J.L. and Tripati, A.E. (2016) Abrupt reorganization of North Pacific and
835 western North American climate during the last deglaciation. Geophysical Research Letters 43,
836 11,796-711,804.https://doi.org/10.1002/2016GL071244.

837 Lora, J.M., Skinner, C.B., Rush, W.D. and Baek, S.H. (2023) The Hydrologic Cycle and
838 Atmospheric Rivers in CESM2 Simulations of the Last Glacial Maximum. Geophysical
839 Research Letters 50, e2023GL104805.https://doi.org/10.1029/2023GL104805.

840 Lowenstein, T., Olson, K., Stewart, B., Mcgee, D., Stroup, J., Hudson, A., Wendt, K., Peaple,
841 M., Feakins, S., Bhattacharya, T. and Lund, S. (2024) Unified 200 kyr paleohydrologic history of
842 the Southern Great Basin: Death Valley, Searles Valley, Owens Valley and the Devils Hole cave.
843 Quaternary Science Reviews 336.10.1016/j.quascirev.2024.108751.

844 McGee, D., Moreno-Chamarro, E., Marshall, J. and Galbraith, E.D. (2018) Western U.S. lake
845 expansions during Heinrich stadials linked to Pacific Hadley circulation. Science Advances 4,
846 10.10.1126/sciadv.aav0118.

847 Menking, K.M., Bischoff, J.L., Fitzpatrick, J.A., Burdette, J.W. and Rye, R.O. (1997)
848 Climatic/Hydrologic Oscillations since 155,000 yr B.P. at Owens Lake, California, Reflected in
849 Abundance and Stable Isotope Composition of Sediment Carbonate. Quaternary Research 48,
850 58-68.10.1006/qres.1997.1898.

851 Mering, J., Arnold, A.J., Chari, L., Lee, H.-I., Lerback, J., Ajoku, O., Ibarra, D.E., Nelson, S.,
852 Farnsworth, A., Valdes, P. and Tripati, A. (2026) Quantifying the impacts of rainfall and
853 evaporation on Lake Bonneville. Science Advances 12, eadw4951.10.1126/sciadv.adw4951.

854 Morrill, C., Lowry, D.P. and Hoell, A. (2018) Thermodynamic and Dynamic Causes of Pluvial
855 Conditions During the Last Glacial Maximum in Western North America. Geophysical Research
856 Letters 45, 335-345.https://doi.org/10.1002/2017GL075807.

857 Moseley, G.E., Edwards, R.L., Wendt, K.A., Cheng, H., Dublyansky, Y., Lu, Y.B., Boch, R. and
858 Spotl, C. (2016) Reconciliation of the Devils Hole climate record with orbital forcing. Science
859 351, 165-168.10.1126/science.aad4132.

860 National Centers for Environmental Information (2020a) U.S. Climate Normals Quick Access-
861 Laketown, UT (USC00424856). National Oceanic and Atmospheric Administration

862 National Centers for Environmental Information (2020b) U.S. Climate Normals Quick Access-
863 Salt Lake City Intl Ap, UT (USW00024127). National Oceanic and Atmospheric Administration

864 Nelson, D.B., Knohl, A., Sachse, D., Schefulss, E. and Kahmen, A. (2017) Sources and
865 abundances of leaf waxes in aerosols in central Europe. Geochimica Et Cosmochimica Acta 198,
866 299-314.10.1016/j.gca.2016.11.018.

867 Osman, M.B., Tierney, J.E., Zhu, J., Tardif, R., Hakim, G.J., King, J.C. and Poulsen, C.J. (2021)
868 Globally resolved surface temperatures since the Last Glacial Maximum. Nature 599, 239-
869 244.10.1038/s41586-021-03984-4.

870 Oster, J.L., Ibarra, D.E., Winnick, M.J. and Maher, K. (2015) Steering of westerly storms over
871 western North America at the Last Glacial Maximum. Nature Geoscience 8, 201-
872 205.10.1038/ngeo2365.

873 Oster, J.L., Macarewich, S., Lofverstrom, M., de Wet, C., Montañez, I., Lora, J.M., Skinner, C.
874 and Tabor, C. (2023) North Atlantic meltwater during Heinrich Stadial 1 drives wetter climate
875 with more atmospheric rivers in western North America. Science Advances 9,
876 eadj2225.doi:10.1126/sciadv.adj2225.

877 Oster, J.L., Montañez, I.P., Sharp, W.D. and Cooper, K.M. (2009) Late Pleistocene California
878 droughts during deglaciation and Arctic warming. Earth and Planetary Science Letters 288, 434-
879 443.https://doi.org/10.1016/j.epsl.2009.10.003.

880 Oviatt, C.G., Currey, D.R. and Sack, D. (1992) Radiocarbon chronology of Lake Bonneville,
881 Eastern Great Basin, USA. Palaeogeography, Palaeoclimatology, Palaeoecology 99, 225-
882 241.https://doi.org/10.1016/0031-0182(92)90017-Y.

883 Oviatt, C.G., Madsen, D.B., Miller, D.M., Thompson, R.S. and McGeehin, J.P. (2015) Early
884 Holocene Great Salt Lake, USA. Quaternary Research 84, 57-68.10.1016/j.yqres.2015.05.001.

885 Oviatt, C.G., Thompson, R.S., Kaufman, D.S., Bright, J. and Forester, R.M. (1999)
886 Reinterpretation of the Burmester core, Bonneville basin, Utah. Quaternary Research 52, 180-
887 184.10.1006/qres.1999.2058.

888 Palacios-Fest, M., Cohen, A., Haskell, B., Valero-Garcés, B., Schnurrenberger, D., Heil, C.,
889 Dean, W., Davis, O., Kruger, N. and Dinter, D. (2000) GLAD1, GSL SITE 4, in:
890 Schnurrenberger, D., Haskell, B. (Eds.), Initial Reports of the Global Lakes Drilling Program.
891 University of Arizona; Limnological Research Center, University of Minnesota; Northern
892 Arizona University; University of Utah; United States Geological Survey; University of Rhode
893 Island, Graduate School of Oceanography, pp. 37-46

894 Peaple, M.D., Bhattacharya, T., Lowenstein, T.K., McGee, D., Olson, K.J., Stroup, J.S., Tierney,
895 J.E. and Feakins, S.J. (2022) Biomarker and Pollen Evidence for Late Pleistocene Pluvials in the
896 Mojave Desert. Paleoceanography and Paleoclimatology 37, 20.10.1029/2022pa004471.

897 Quirk, B.J., Moore, J.R., Laabs, B.J.C., Caffee, M.W. and Plummer, M.A. (2018) Termination II,
898 Last Glacial Maximum, and Lateglacial chronologies and paleoclimate from Big Cottonwood
899 Canyon, Wasatch Mountains, Utah. GSA Bulletin 130, 1889-1902.10.1130/B31967.1.

900 Reheis, M.C. (1999) Highest Pluvial-Lake Shorelines and Pleistocene Climate of the Western
901 Great Basin. Quaternary Research 52, 196-205.https://doi.org/10.1006/qres.1999.2064.

902 Reheis, M.C., Adams, K.D., Oviatt, C.G. and Bacon, S.N. (2014) Pluvial lakes in the Great
903 Basin of the western United States—a view from the outcrop. Quaternary Science Reviews 97,
904 33-57.https://doi.org/10.1016/j.quascirev.2014.04.012.

905 Rolph, G., Stein, A. and Stunder, B. (2017) Real-time Environmental Applications and Display
906 sYstem: READY. Environmental Modelling & Software 95, 210-
907 228.https://doi.org/10.1016/j.envsoft.2017.06.025.

908 Rosenbaum, J., Dean, W., Haskell, B., Valero-Garcés, B., Kaufman, D.S., Andersen, R.S.,
909 Bright, J., Schnurrenberger, D., Heil, C., Skipp, G., Honke, J. and Palcios-Fest, M. (2000)

GLAD1, BEAR LAKE SITE 1, in: Schnurrenberger, D., Haskell, B. (Eds.), Initial Reports of the Global Lakes Drilling Program. University of Arizona, Limnological Research Center, University of Minnesota, Northern Arizona University, University of Utah, United States Geological Survey, University of Rhode Island Graduate School of Oceanography, pp. 47-65

So, R.T., Ibarra, D.E., Tierney, J.E., Jagniecki, E., Lowenstein, T.K., Jost, A.B., Olson, K.J., McGee, D. and Feakins, S.J. (2025) NOAA/WDS Paleoclimatology - Great Salt Lake and Bear Lake Plant Waxes Data Pleistocene to Present [Dataset], NOAA National Centers for Environmental Information.10.25921/4wmd-yj23.

So, R.T., Ibarra, D.E., Tierney, J.E., Jagniecki, E., Lowenstein, T.K., Jost, A.B., Olson, K.J., McGee, D. and Feakins, S.J. (2026) Biomarker-based limnology of Great Salt Lake over the last two glacial cycles. ESS Open Archive.10.22541/essoar.176745549.94743633/v2.

Stein, A.F., Draxler, R.R., Rolph, G.D., Stunder, B.J.B., Cohen, M.D. and Ngan, F. (2015) NOAA's HYSPLIT Atmospheric Transport and Dispersion Modeling System. Bulletin of the American Meteorological Society 96, 2059-2077.https://doi.org/10.1175/BAMS-D-14-00110.1.

Tabor, C., Lofverstrom, M., Oster, J.L., Wortham, B., de Wet, C., Montañez, I., Rhoades, A., Zarzycki, C., He, C. and Liu, Z. (2021) A mechanistic understanding of oxygen isotopic changes in the Western United States at the Last Glacial Maximum. Quaternary Science Reviews 274, 107255.https://doi.org/10.1016/j.quascirev.2021.107255.

Tierney, J.E., Zhu, J., King, J., Malevich, S.B., Hakim, G.J. and Poulsen, C.J. (2020) Glacial cooling and climate sensitivity revisited. Nature 584, 569-573.10.1038/s41586-020-2617-x.

Todd, V., Shanahan, T. and Johnson, B. (2025) Hydroclimate and Ecosystem Changes in the Colorado Rocky Mountains Since the Last Glacial Maximum. Paleoceanography and Paleoclimatology 40.10.1029/2024PA005049.

Veals, P.G., Pletcher, M., Schwartz, A.J., Chase, R.J., Harnos, K., Correia, J., Wessler, M.E. and Steenburgh, W.J. (2025) Predicting Snow-to-Liquid Ratio in the Mountains of the Western United States. Weather and Forecasting.https://doi.org/10.1175/WAF-D-24-0233.1.

936 Wackerbarth, A., Scholz, D., Fohlmeister, J. and Mangini, A. (2010) Modelling the $\delta^{18}O$ value of
937 cave drip water and speleothem calcite. Earth and Planetary Science Letters 299, 387-
938 397.https://doi.org/10.1016/j.epsl.2010.09.019.

939 Wagner, J.D.M., Cole, J.E., Beck, J.W., Patchett, P.J., Henderson, G.M. and Barnett, H.R. (2010)
940 Moisture variability in the southwestern United States linked to abrupt glacial climate change.
941 Nature Geoscience 3, 110-113.10.1038/ngeo707.

942 Waterisotopes Database (2017a) Site Name: at DOT bldg at snowmobile park Hwy 39.
943 http://waterisotopesDB.org, pp. Accessed July 26, 2025

944 Waterisotopes Database (2017b) Site Name: at Huntsville Library. http://waterisotopesDB.org,
945 pp. Accessed July 26, 2025

946 Waterisotopes Database (2017c) Site Name: at Pizzel Spring pumphouse.
947 http://waterisotopesDB.org, pp. Accessed July 26, 2025

948 Waterisotopes Database (2017d) Site Name: at Powder Mountain top of Hidden Lake lift.
949 http://waterisotopesDB.org, pp. Accessed July 26, 2025

950 Waterisotopes Database (2024) Site Name: Fredrick Albert Sutton Building. Waterisotopes.org,
951 pp. Accessed July 26, 2025

952 Waterisotopes Database (2025a) Interpolated data at Bear Lake, in: Bowen, G. (Ed.).
953 Waterisotopes.org, pp. Accessed Aug 5, 2025. Latitude: 2041.2095, Longitude: -2111.2031,
954 Elevation: 1806 masl.

955 Waterisotopes Database (2025b) Interpolated data at Great Salt Lake, in: Bowen, G. (Ed.).
956 Waterisotopes.org, pp. Accessed Aug 5, 2025. Latitude: 2041.2013, Longitude: -2112.2056,
957 Elevation: 1280 masl.

958 Wendt, K.A., Carolin, S., Buizert, C., Steidle, S.D., Edwards, R.L., Moseley, G.E., Dublyansky,
959 Y., Cheng, H., He, C., Warner, M.S.C. and Spötl, C. (2025) Controls on the southwest USA
960 hydroclimate over the last six glacial-interglacial cycles. Nature Communications 16,
961 10007.10.1038/s41467-025-64963-1.

962 Wendt, K.A., Dublyansky, Y.V., Moseley, G.E., Edwards, R.L., Cheng, H. and Spotl, C. (2018)
963 Moisture availability in the southwest United States over the last three glacial-interglacial cycles.
964 Science Advances 4, 8.10.1126/sciadv.aau1375.

965 Winnick, M.J., Chamberlain, C.P., Caves, J.K. and Welker, J.M. (2014) Quantifying the isotopic
966 'continental effect'. Earth and Planetary Science Letters 406, 123-
967 133.https://doi.org/10.1016/j.epsl.2014.09.005.

968 Winograd, I.J., Coplen, T.B., Landwehr, J.M., Riggs, A.C., Ludwig, K.R., Szabo, B.J., Kolesar,
969 P.T. and Revesz, K.M. (1992) Continuous 500,000-Year Climate Record from Vein Calcite in
970 Devils Hole, Nevada. Science 258, 255-260.10.1126/science.258.5080.255.

971 Winograd, I.J. and Thordarson, W. (1975) Hydrogeologic and hydrochemical framework, south-
972 central Great Basin, Nevada-California, with special reference to the Nevada Test Site,
973 Professional Paper.10.3133/pp712C.

974 Wise, E.K. (2010) Spatiotemporal variability of the precipitation dipole transition zone in the
975 western United States. Geophysical Research Letters 37.https://doi.org/10.1029/2009GL042193.

976 Wong, C.I., Potter, G.L., Montañez, I.P., Otto-Bliesner, B.L., Behling, P. and Oster, J.L. (2016)
977 Evolution of moisture transport to the western U.S. during the last deglaciation. Geophysical
978 Research Letters 43, 3468-3477.https://doi.org/10.1002/2016GL068389.

979 Zhu, J., Liu, Z., Brady, E., Otto-Bliesner, B., Zhang, J., Noone, D., Tomas, R., Nusbaumer, J.,
980 Wong, T., Jahn, A. and Tabor, C. (2017) Reduced ENSO variability at the LGM revealed by an
981 isotope-enabled Earth system model. Geophysical Research Letters 44, 6984-
982 6992.https://doi.org/10.1002/2017GL073406.
983

984 **References From the Supporting Information**

985 Aichner, B., Herzschuh, U. and Wilkes, H. (2010) Influence of aquatic macrophytes on the stable
986 carbon isotopic signatures of sedimentary organic matter in lakes on the Tibetan Plateau. Organic
987 Geochemistry 41, 706-718.10.1016/j.orggeochem.2010.02.002.

988 Asmerom, Y., Polyak, V.J. and Burns, S.J. (2010) Variable winter moisture in the southwestern
989 United States linked to rapid glacial climate shifts. Nature Geoscience 3, 114-
990 117.10.1038/ngeo754.

991 Balch, D.P., Cohen, A.S., Schnurrenberger, D.W., Haskell, B.J., Garces, B.L.V., Beck, J.W.,
992 Cheng, H. and Edwards, R.L. (2005) Ecosystem and paleohydrological response to Quaternary
993 climate change in the Bonneville Basin, Utah. Palaeogeography Palaeoclimatology
994 Palaeoecology 221, 99-122.10.1016/j.palaeo.2005.01.013.

995 Colman, S.M., Kaufman, D.S., Bright, J., Heil, C., King, J.W., Dean, W.E., Rosenbaum, J.G.,
996 Forester, R.M., Bischoff, J.L., Perkins, M. and McGeehin, J.P. (2006) Age model for a
997 continuous, ca 250-ka Quaternary lacustrine record from Bear Lake, Utah-Idaho. Quaternary
998 Science Reviews 25, 2271-2282.10.1016/j.quascirev.2005.10.015.

999 Conte, M. and Weber, J. (2002) Long-range atmospheric transport of terrestrial biomarkers to the
1000 western North Atlantic. Global Biogeochemical Cycles 16.10.1029/2002gb001922.

1001 Eggleston, S., Schmitt, J., Bereiter, B., Schneider, R. and Fischer, H. (2016) Evolution of the
1002 stable carbon isotope composition of atmospheric CO2 over the last glacial cycle.
1003 Paleoceanography 31, 434-452.10.1002/2015pa002874.

1004 Feakins, S.J. and Sessions, A.L. (2010) Controls on the D/H ratios of plant leaf waxes in an arid
1005 ecosystem. Geochimica Et Cosmochimica Acta 74, 2128-2141.10.1016/j.gca.2010.01.016.

1006 Freeman, K.H. and Pancost, R.D. (2014) Biomarkers for Terrestrial Plants and Climate, in:
1007 Holland, H.D., Turekian, K.K. (Eds.), Treatise on Geochemistry (Second Edition). Elsevier,
1008 Oxford, pp. 395-416.

1009 Friedman, I., Harris, J.M., Smith, G.I. and Johnson, C.A. (2002) Stable isotope composition of
1010 waters in the Great Basin, United States 1. Air-mass trajectories. Journal of Geophysical
1011 Research: Atmospheres 107, ACL 14-11-ACL 14-14.https://doi.org/10.1029/2001JD000565.

1012 Global Network of Isotopes in Precipitation (2022) Salt Lake City (Utah), International Atomic
1013 Energy Agency

1014 Ibarra, D.E., Oster, J.L., Winnick, M.J., Rugenstein, J.K.C., Byrne, M.P. and Chamberlain, C.P.
1015 (2018) Warm and cold wet states in the western United States during the Pliocene-Pleistocene.
1016 Geology 46, 355-358.10.1130/G39962.1.

1017 Lachniet, M. (2016) A Speleothem Record of Great Basin Paleoclimate: The Leviathan
1018 Chronology, Nevada, Lake Bonneville: A Scientific Update. Elsevier Science BV, Sara
1019 Burgerhartstraat 25, PO box 211, 1000 AE Amsterdam, Netherlands, pp. 551-569.10.1016/b978-
1020 0-444-63590-7.00020-2.

1021 Lundeen, Z., Brunelle, A., Burns, S.J., Polyak, V. and Asmerom, Y. (2013) A speleothem record
1022 of Holocene paleoclimate from the northern Wasatch Mountains, southeast Idaho, USA.
1023 Quaternary International 310, 83-95.https://doi.org/10.1016/j.quaint.2013.03.018.

1024 Matsubara, Y. and Howard, A.D. (2009) A spatially explicit model of runoff, evaporation, and
1025 lake extent: Application to modern and late Pleistocene lakes in the Great Basin region, western
1026 United States. Water Resources Research 45.https://doi.org/10.1029/2007WR005953.

1027 National Centers for Environmental Information (2020a) U.S. Climate Normals Quick Access-
1028 Laketown, UT (USC00424856). National Oceanic and Atmospheric Administration

1029 National Centers for Environmental Information (2020b) U.S. Climate Normals Quick Access-
1030 Salt Lake City Intl Ap, UT (USW00024127). National Oceanic and Atmospheric Administration

1031 Nelson, D.B., Knohl, A., Sachse, D., Schefulss, E. and Kahmen, A. (2017) Sources and
1032 abundances of leaf waxes in aerosols in central Europe. Geochimica Et Cosmochimica Acta 198,
1033 299-314.10.1016/j.gca.2016.11.018.

1034 Oster, J.L., Montañez, I.P., Santare, L.R., Sharp, W.D., Wong, C. and Cooper, K.M. (2015)
1035 Stalagmite records of hydroclimate in central California during termination 1. Quaternary
1036 Science Reviews 127, 199-214.https://doi.org/10.1016/j.quascirev.2015.07.027.

1037 Oster, J.L., Weisman, I.E. and Sharp, W.D. (2020) Multi-proxy stalagmite records from northern
1038 California reveal dynamic patterns of regional hydroclimate over the last glacial cycle.
1039 Quaternary Science Reviews 241, 106411.https://doi.org/10.1016/j.quascirev.2020.106411.

1040 Oviatt, C.G., Thompson, R.S., Kaufman, D.S., Bright, J. and Forester, R.M. (1999)
1041 Reinterpretation of the Burmester core, Bonneville basin, Utah. Quaternary Research 52, 180-
1042 184.10.1006/qres.1999.2058.

1043 Rolph, G., Stein, A. and Stunder, B. (2017) Real-time Environmental Applications and Display
1044 sYstem: READY. Environmental Modelling & Software 95, 210-
1045 228.https://doi.org/10.1016/j.envsoft.2017.06.025.

1046 So, R.T., Ibarra, D.E., Tierney, J.E., Jagniecki, E., Lowenstein, T.K., Jost, A.B., Olson, K.J.,
1047 McGee, D. and Feakins, S.J. (2026) Biomarker-based limnology of Great Salt Lake over the last
1048 two glacial cycles. ESS Open Archive.10.22541/essoar.176745549.94743633/v2.

1049 Stein, A.F., Draxler, R.R., Rolph, G.D., Stunder, B.J.B., Cohen, M.D. and Ngan, F. (2015)
1050 NOAA's HYSPLIT Atmospheric Transport and Dispersion Modeling System. Bulletin of the
1051 American Meteorological Society 96, 2059-2077.https://doi.org/10.1175/BAMS-D-14-00110.1.

1052 Wagner, J.D.M., Cole, J.E., Beck, J.W., Patchett, P.J., Henderson, G.M. and Barnett, H.R. (2010)
1053 Moisture variability in the southwestern United States linked to abrupt glacial climate change.
1054 Nature Geoscience 3, 110-113.10.1038/ngeo707.

1055 Waterisotopes Database (2017a) Site Name: at DOT bldg at snowmobile park Hwy 39.
1056 http://waterisotopesDB.org, pp. Accessed July 26, 2025

1057 Waterisotopes Database (2017b) Site Name: at Huntsville Library. http://waterisotopesDB.org,
1058 pp. Accessed July 26, 2025

1059 Waterisotopes Database (2017c) Site Name: at Pizzel Spring pumphouse.
1060 http://waterisotopesDB.org, pp. Accessed July 26, 2025

1061 Waterisotopes Database (2017d) Site Name: at Powder Mountain top of Hidden Lake lift.
1062 http://waterisotopesDB.org, pp. Accessed July 26, 2025

1063 Waterisotopes Database (2024) Site Name: Fredrick Albert Sutton Building. Waterisotopes.org,
1064 pp. Accessed July 26, 2025

1065 Waterisotopes Database (2025a) Interpolated data at Bear Lake, in: Bowen, G. (Ed.).
1066 Waterisotopes.org, pp. Accessed Aug 5, 2025. Latitude: 2041.2095, Longitude: -2111.2031,
1067 Elevation: 1806 masl.

1068 Waterisotopes Database (2025b) Interpolated data at Great Salt Lake, in: Bowen, G. (Ed.).
1069 Waterisotopes.org, pp. Accessed Aug 5, 2025. Latitude: 2041.2013, Longitude: -2112.2056,
1070 Elevation: 1280 masl.

1071 Wendt, K.A., Carolin, S., Buizert, C., Steidle, S.D., Edwards, R.L., Moseley, G.E., Dublyansky,
1072 Y., Cheng, H., He, C., Warner, M.S.C. and Spötl, C. (2025) Controls on the southwest USA
1073 hydroclimate over the last six glacial-interglacial cycles. Nature Communications 16,
1074 10007.10.1038/s41467-025-64963-1.

Figure 1.

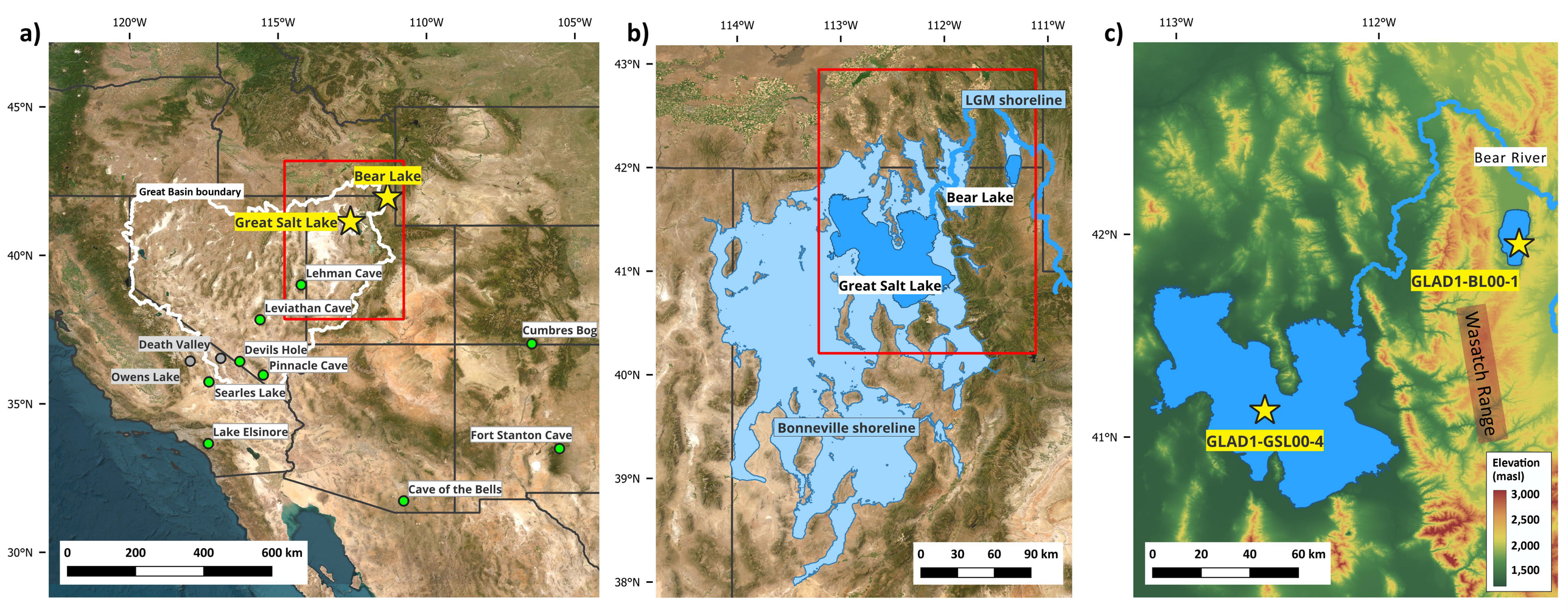
a)
120°W
115°W
110°W
105°W
45°N
40°N
35°N
30°N
Bear Lake
Great Basin boundary
Great Salt Lake
Lehman Cave
Leviathan Cave
Cumbres Bog
Death Valley
Devils Hole
Pinnacle Cave
Owens Lake
Searles Lake
Lake Elsinore
Fort Stanton Cave
Cave of the Bells
0 200 400 600 km
b)
114°W
113°W
112°W
111°W
43°N
42°N
41°N
40°N
39°N
38°N
LGM shoreline
Bear Lake
Great Salt Lake
Bonneville shoreline
0 30 60 90 km
c)
113°W
112°W
42°N
41°N
Bear River
GLAD1-BL00-1
Wasatch Range
GLAD1-GSL00-4
Elevation (masl)
3,000
2,500
2,000
1,500
0 20 40 60 km

Figure 2.

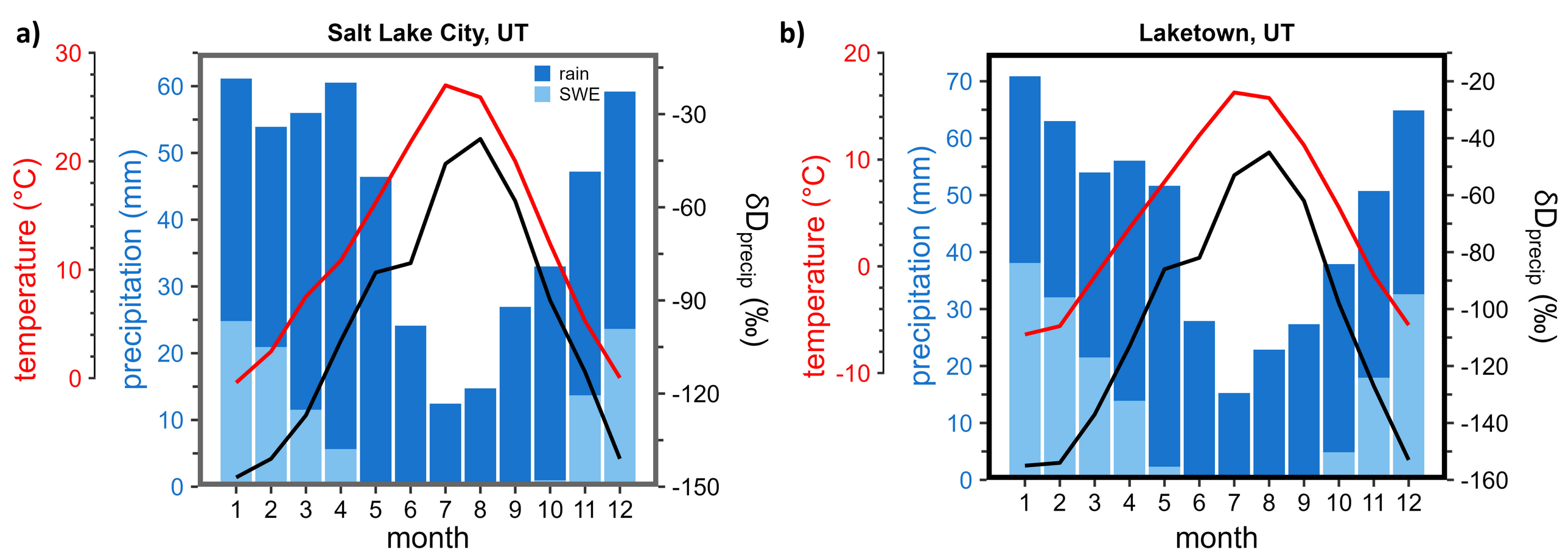
a)
Salt Lake City, UT
rain
SWE
temperature (°C)
precipitation (mm)
δDprecip (‰)
month
b)
Laketown, UT
temperature (°C)
precipitation (mm)
δDprecip (‰)
month

Figure 3.

a)

1 MIS 2 MIS 3 4 MIS 5 MIS 6 MIS 7a-c 7d 7e

Dome C pCO_2

benthic foram $\delta^{18}O$

$\delta^{18}O_{benthic}$ (‰ VPDB)

3

4

5

280

240

200

160

pCO_2 (ppm)

b)

δD_{precip} (‰ VSMOW)

-100

-120

-140

-160

Great Salt Lake

salt

Bonneville

salt

Little Valley

20

15

10

5

0

Dry taxa %

c)

-100

-120

-140

-160

Bear Lake

30

20

10

0

Dry taxa %

d)

-80

-100

-120

-140

Searles Lake

salt

salt

60

40

20

0

Dry taxa %

0 40 80 120 160 200 240

Age (ka)

0 40 80 120 160 200 240

Age (ka)

Figure 4.

a)

Plant wax

1 | MIS 2 | MIS 3 | 4 | MIS 5 | MIS 6 | MIS 7a-c | 7d | 7e

δD_{precip} (‰ VSMOW)

-80
-100
-120
-140
-160

Bear Lake
Great Salt Lake
Searles Lake

b)

Cave

$\delta^{18}O$ (‰ VPDB)

-10
-12
-14
-16

Leviathan comp.
Leviathan
Lehman
Pinnacle

Devil's Hole
DH2

0
40
80
120
160
200
240

Age (ka)

Figure 5.

0
-40
-80
-120
-160
δD (‰ VSMOW)
alkane
alkanoic acid
carbonate
interglacial
glacial
T1
T2
n = 10
n = 39
Feakins et al. (2019)
1, 4
4, 4
Peaple et al. (2022)
37, 55
6, 57
Wendt et al. (2025)
236, 38
41, 27
Lachniet et al. (2016)
11
40
Wagner et al. (2010)
4, 4
1, 5
this study
9, 5
2, 5
this study
71
4
Todd et al. (2025)
3
142
Asmerom et al. (2010)
Elsinore
Searles
Devils Hole
Leviathan composite
Cave of the Bells
Great Salt Lake
Bear Lake
Cumbres Bog
Fort Stanton
distance from shore (W to E)

Figure 6.

a)

PI δD_{precip}

b)

LGM δD_{precip}

50°N
45°N
40°N
35°N
30°N

130°W 125°W 120°W 115°W 110°W 105°W 100°W

−20
−40
−60
−80
−100
−120
−140
−160
−180

δD (% VSMOW)

c)

LGM−PI $\Delta\delta D_{precip}$

50
45
40
35
30

130°W 125°W 120°W 115°W 110°W 105°W 100°W

0
−10
−20
−30
−40
−50
−60

ΔδD (% VSMOW)

alkane
alkanoic acid
carbonate

Figure 7.

Model vs. Proxy LGM-PI δD difference

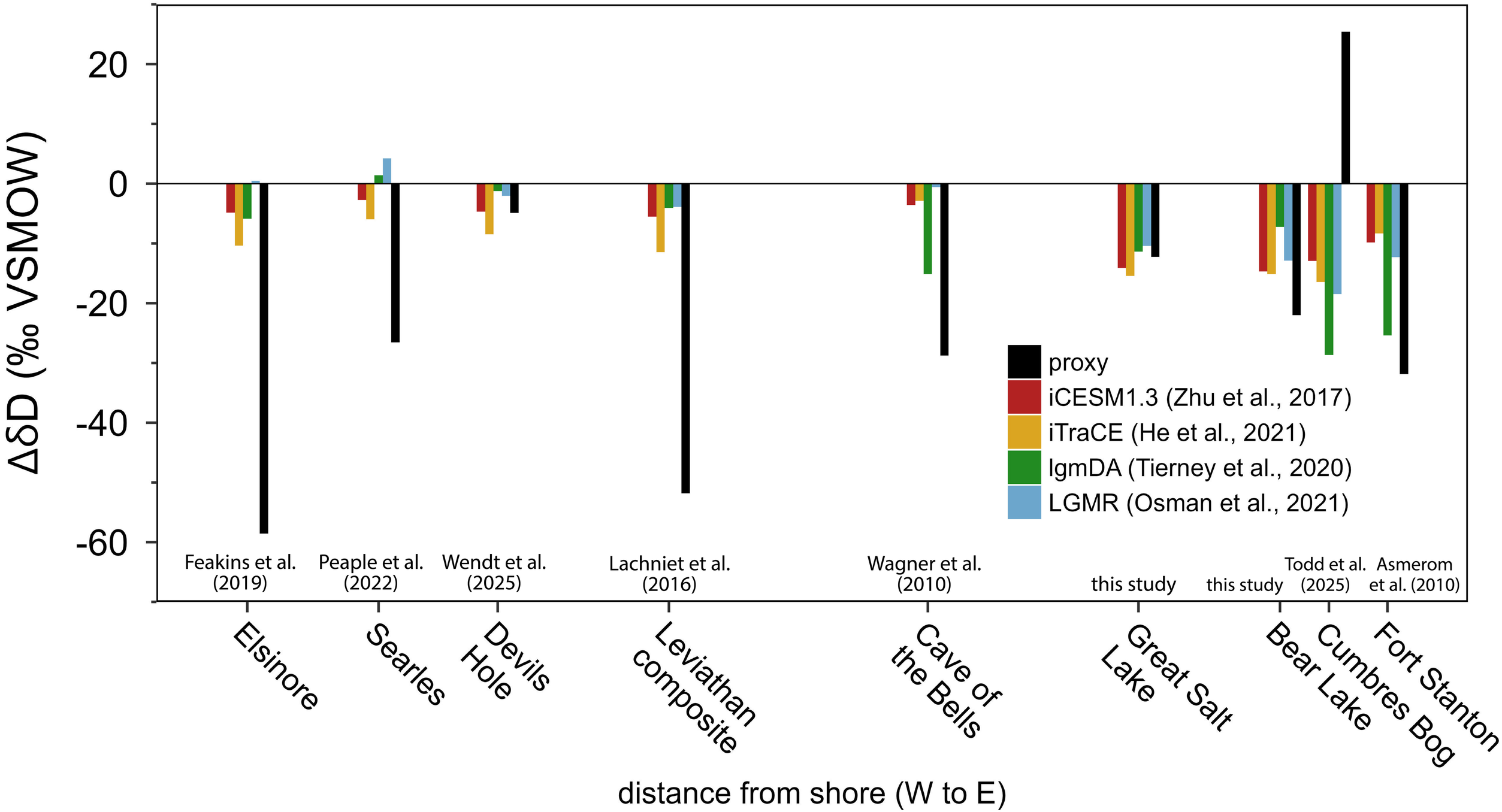

AGU PUBLICATIONS

Supporting Information for

Plant wax isotopic reconstructions reveal thermodynamic drivers of hydroclimate over the last two glacial cycles at Great Salt Lake and Bear Lake, Utah

Rachel T. So[1*], Daniel E. Ibarra[2], Jessica E. Tierney[3], Elliot Jagniecki[4], Tim K. Lowenstein[5], Adam Jost[6], Kristian Olson[7], David McGee[6], and Sarah J. Feakins[1]

[1]Department of Earth Sciences, University of Southern California, Los Angeles, CA 90089, USA.
[2]Department of Earth, Environmental and Planetary Science, Brown University, Providence, RI 02906, USA.
[3]Department of Geoscience, University of Arizona, Tucson, AZ 85721, USA.
[4]Utah Geological Survey, Salt Lake City, UT 84114, USA.
[5]Department of Earth Sciences, Binghamton University, Binghamton, NY 13902, USA.
[6]Department of Earth, Atmospheric, and Planetary Sciences, Massachusetts Institute of Technology, Cambridge, MA, USA
[7]Department of Geology, Alfred University, Alfred, NY, USA
Corresponding author: Rachel T. So (rtso@usc.edu)

Contents of this file

Introduction

The supporting information associated with the manuscript referenced above includes ten supplementary text sections and twenty-two supplementary figures. Text S1 provides details of the modern sampling of plants, soils and catchment sediments. Text S2 provides the alkyl lipid quantification methods. Text S3 provides the alkyl lipid stable isotopic analyses methods. Text S4 provides the results of the modern sampling. Text S5 reports the downcore quantification of alkyl lipids. Text S6 reports the δD results for downcore *n*-alkanes. Text S7 reports the $\delta^{13}C$ results for downcore *n*-alkanes. Text S8 reports the compound specific isotopic results for downcore fatty acids that were determined to be dominated by aquatic production. Text S9 discusses the provenance of lipids transported into the lake sediments. Text S10 describes $\varepsilon_{wax/water}$ variability downcore GLAD1-BL00-1 when adjusted based on the pollen composition. Text S11 estimates the influence changes in snow proportion have on the interpretation of signals in the plant wax record. Text S12 determines mixing model estimates for storm track sourcing interpretation of signals in the plant wax record. Figure S1 is a map of air mass trajectories at~500 hPa to Great Salt Lake and Bear Lake during the winter (December, January, February) and summer (June, July, August) seasons. Figure S2 shows the age model for the Great Salt Lake sediment core GLAD1-GSL00-4 and Figure S3 shows the age model for the Bear Lake sediment core GLAD1-BL00-1. Figure S4 is a map of modern sampling sites in the Bear Lake catchment. Figure S5 shows the chain length distribution of alkyl lipids for the

modern plants sampled, and Figure S6 shows their summed abundance by species. Figure S7 shows the chain length distribution of alkyl lipids in modern sediments and soils. Figure S8 shows the $\delta^{13}C$ results for modern plants and Figure S9 shows the corresponding results for modern sediments and soils. Figure S10 shows the δD results for modern plants and Figure S11 shows the corresponding results for modern sediments and soils. Figure S12 shows cross plots of δD versus $\delta^{13}C$ for *n*-alkanes in modern plants while Figure S13 shows the same for fatty acids in modern plants. Figure S14 shows the downcore alkyl lipid abundances at Great Salt Lake and Bear Lake while Figures S15 shows their chain length distributions. Figures S16 shows the downcore compound specific isotopic results of *n*-alkanes at both lakes, and Figure S17 shows the same for fatty acids. Figure S18 shows a correlation matrix of R values comparing regional precipitation isotope records. Figure S19 shows the temperature-δD relationship of modern precipitation at Salt Lake City. Figure S20 shows regional speleothem $\delta^{18}O$ records, including short-spanning Holocene archives to archives spanning the last two glacial cycles. Figure S21 is a comparison of seasonal patterns in monthly temperature, precipitation, and δD_{precip} between iCESM1.3 model outputs and modern observations at Great Salt Lake and Bear Lake. Figure S22 are maps showing iCESM1.3 simulated pre-industrial and Last Glacial Maximum precipitation amounts in the western US. Table S1 is the list of sampling sites in the modern Bear Lake catchment.

Supplementary Text

Text S1. Modern plant and catchment sampling

To complement the downcore reconstructions from the two lakes presented in the main paper, we additionally collected modern plant, soil and sediment samples from the Bear Lake catchment, reported here. A suite of plant leaves (n = 32), surface lake/stream sediments (n = 15), and soils (n = 5) were collected at 25 locations around the Bear Lake catchment over a 3-day period in Aug 2023 (**Figure S2**, **Table S1**). Plant leaves were collected at various times throughout the day and stored in Whirlpak bags at room temperature until they could be transported into a -20°C freezer. For purposes of comparison, as we could not identify plants down to the species level, plants were broadly divided into ten categories based on genus or growth form (*Artemisia*, asters, *Salix*, shrubs, graminoid, *Schoenoplectus*, *Pinus*, *Picea*, *Abies*). Surface sediments were collected from the Bear Lake lakebed (n = 4) and from the beds of connecting streams (n = 11) using a shovel while standing at the shore. An adjacent soil was sometimes also collected. As with the plant samples, sediments and soils were stored in Whirlpak bags at room temperature until they were moved into a -20°C freezer. For sample processing, fresh plant material was freeze-dried then cut into sub-centimeter sized fragments using solvent-cleaned scissors. Their total lipid extracts (TLE) were obtained by immersing plant material in either 9:1 dichloromethane (DCM):methanol (MeOH) or in DCM. Soil and sediment samples were processed in the same way as lake core sediments reported in the main text.

Text S2. *n*-Alkane and *n*-alkanoic acid quantification

n-Alkanes and FAMEs were quantified using either 1) an Agilent 6890 Gas Chromatograph (GC) (30 m x 0.25 mm column, 0.25 μm coating Rxi®-5ms) with an Agilent 7683 programmable autosampler and connected to an Agilent 5973 MSD mass spectrometer (MS) and flame ionization detector (FID), or 2) a Thermo Scientific TRACE 1610 GC (same column) with an AI 1610 autosampler connected to a Thermo Scientific ISQ 7610 single quadrupole MS and FID. Compounds were identified by their retention time, mass spectrum, and comparison to an in-house standard containing known concentrations of *n*-alkanes and FAMEs. They were then quantified using FID peak areas of the same in-house standard, with separate response curves

for each compound class with an uncertainty of <4% based on replicate standards. Average chain length (ACL) was calculated with the following equation:

$$ACL = \frac{\Sigma n \times [C_n]}{\Sigma [C_n]}$$

where the chain length (*n*) refers to the C_{25} to C_{35} *n*-alkanes and C_{24} to C_{34} *n*-alkanoic acids. We also measured the carbon preference index (CPI):

$$CPI = \frac{2\Sigma [C_n]}{\Sigma [C_{n-1}] + \Sigma [C_{n+1}]}$$

where *n* = 25, 27, 29, 31, and 33 for the *n*-alkanes and *n* = 24, 26, 28, 30, and 32 for the *n*-alkanoic acids.

Text S3. Alkyl lipid stable isotopic analyses

For all samples, *n*-alkane and *n*-alkanoic acid stable carbon isotopic compositions were analyzed using a Thermo Scientific TRACE 1610 GC (30 m x 0.25 mm column, 0.25 µm coating Rxi®-5ms) connected to a Thermo Scientific Delta Q IRMS with a Triplus RSH Smart Autosampler, a Conflo IV, and a GC Isolink II at the University of Southern California. CO_2 linearity was monitored daily and averaged –0.4 ppm/nÅ (1σ = 0.4 ppm/nÅ) over a range of 1-8 V. Each sample run was bracketed with CO_2 peaks, two of which were used for normalization between standard and sample runs. All $\delta^{13}C$ were normalized to the international reference standard Vienna Pee Dee Belemnite (VPDB) using an external standard. The external standard contains a mixture of 15 *n*-alkanes (C_{16} to C_{30}) with $\delta^{13}C$ values ranging from –25.9‰ to –33.7‰ (A6 mix supplied by A. Schimmelmann, Indiana University, USA). The RMS uncertainty (accuracy and precision) was 0.6‰ (1σ = 0.4‰). Measurements were replicated at least twice with instrument precision of 0.3‰ (1σ = 0.4‰). *n*-Alkanoic acid stable hydrogen isotopic compositions were measured following the method for all other samples outlined in section 2.3 of the main text. Stable isotope values of n-alkanoic acids were corrected to account for the added methyl group during methylation, determined by derivatization of phthalic acid of known isotopic composition (also supplied by A. Schimmelmann).

Text S4. Modern plant, sediment, and soil results

Modern plant leaves yielded long-chain *n*-alkane abundance (ΣC_{25}-C_{35} Alk) averaging 541.8 µg/gdw (1σ = 714.5 µg/gdw) and long-chain *n*-alkanoic acid abundance (ΣC_{24}-C_{34} FA) of 243.1 µg/gdw (1σ = 297.5 µg/gdw) (**Figure S5**, **S6**). Except for two gymnosperm individuals (*Picea* sp. and *Pinus* sp.), all plant samples had an *n*-alkane CPI (CPI_{alk}) >4, characteristic of fresh vegetation (Freeman and Pancost, 2014 and references therein). For *n*-alkanoic acid CPI (CPI_{FA}), only one plant (*Populus* sp.) had a CPI_{FA} <4. All lipid compounds in plant samples measured for $\delta^{13}C$ fell in the range of –42.1‰ to –27.7‰ (**Figure S8**). Sediments and soils had a smaller range in $\delta^{13}C$ values, at –37.0‰ to –28.1‰ (**Figure S9**), which fully fell within the range of plant material. Plant wax δD values had a large ~160‰ range in values, spanning –323‰ to –163‰ (**Figure S10**). Sediments and soils had a slightly smaller ~130‰ range in values with slightly higher values than plants, spanning –292‰ to –159‰ (**Figure S11**).

Text S5. Downcore *n*-alkane and *n*-alkanoic acid abundances

In GLAD1-GSL00-4, ΣC_{25}-C_{35} Alk averaged 6.8 µg/gdw (1σ = 6.9 µg/gdw) while CPI_{alk} and ACL_{alk} averaged 7.0 (1σ = 1.8) and 28.6 (1σ = 0.2) respectively (**Figure S14b**). ΣC_{24}-C_{34} FA was

an order of magnitude higher, averaging 55.7 µg/gdw (1σ = 95.7 µg/gdw) with a CPI_{FA} and ACL_{FA} of 7.2 (1σ = 2.2) and 26.6 (1σ = 0.4) respectively (**Figure S14a**). In GLAD1-BL00-1, ΣC_{25}-C_{35} Alk averaged 5.5 µg/gdw (1σ = 3.6 µg/gdw), CPI_{alk} at 7.8 (1σ = 1.1), and ACL_{alk} at 28.5 (1σ = 0.5) (**Figure S14d**). ΣC_{24}-C_{34} FA averaged 30.5 µg/gdw (1σ = 23.1 µg/gdw), CPI_{FA} at 5.9 (1σ = 1.6), and ACL_{FA} at 26.9 (1σ = 0.3) (**Figure S14c**). For both compound classes at both lakes, individual chain lengths showed similar patterns in abundances downcore (**Figure S14**). Further, ΣC_{25}-C_{35} Alk and ΣC_{24}-C_{34} FA significantly correlated at both lakes (Bear Lake: R^2 = 0.63, p << 0.05; Great Salt Lake: R^2 = 0.52, p << 0.05). At both lakes, ΣC_{24}-C_{34} FA was 7-8 times higher than ΣC_{25}-C_{35} Alk, and we do not observe a glacial-interglacial signal in the abundances of either compound class. In addition to plant wax abundances, we report the δD and $\delta^{13}C$ of these compounds in the following text sections. We focus on the most abundant long-chain compounds for each compound class–C_{27}, C_{29}, and C_{31} for *n*-alkanes, and C_{26}, C_{28}, and C_{30} for *n*-alkanoic acids. Due to highly divergent concentrations of individual *n*-alkanoic acids, we focused on measuring the stable isotope values of C_{28} and C_{30} alkanoic acids and did not measure them for the C_{26} alkanoic acid (which had significantly higher concentrations).

Text S6. Downcore *n*-alkane δD

Here, we report the *n*-alkane δD values measured in the two lake sediment cores. Downcore GLAD1-GSL00-4, C_{27}, C_{29}, and C_{31} alkane δD ranged between approximately –230‰ to –200‰, –225‰ to –200‰, and –235‰ to –205‰ (**Figure S17a**). For GLAD1-BL00-1, C_{27}, C_{29}, and C_{31} alkane δD ranged between approximately –240‰ to –190‰, –240‰ to –200‰, and –240‰ to –200‰ (**Figure S17b**). Discussion of the *n*-alkane δD records of both lakes, after conversion to δD_{precip}, is available in the main text.

Text S7. Downcore *n*-alkane $\delta^{13}C$

In GLAD1-GSL00-4, C_{27}, C_{29}, and C_{31} alkane $\delta^{13}C$ averaged –28.7‰ (1σ = 1.4‰), –30.6‰ (1σ = 1.2‰), and –31.0‰ (1σ = 1.0‰) (**Figure S17c**). Downcore GLAD1-BL00-1, C_{27}, C_{29}, and C_{31} alkane $\delta^{13}C$ averaged –29.9‰ (1σ = 1.1‰), –31.7‰ (1σ = 1.1‰), and –32.8‰ (1σ = 1.2‰) (**Figure S17d**). There are no consistent glacial-interglacial signals in the carbon isotopic composition of plant waxes, which range over 4‰ with differences between chain lengths that suggest changes in vegetation inputs. Atmospheric CO_2 $\delta^{13}C$ varied <0.6‰ over the last 160 ky (Eggleston et al., 2016) and thus cannot explain the ~4‰ range. Low $\delta^{13}C$ values in the C_{31} *n*-alkanes (but not other chain lengths) at Great Salt Lake preceding/during deep lake phases coinciding with glacial terminations 1 and 2 (Balch et al., 2005). Pluvial conditions drove Great Salt Lake highstands during MIS 2 and MIS 6 which would imply decreased water stress (Ibarra et al., 2018; Matsubara and Howard, 2009; Oviatt et al., 1999). Greater stomatal conductivity permits greater fractionation and lower alkane $\delta^{13}C$. During glacials lower atmospheric pCO_2 and greater water availability could both drive increased fractionation. However, the higher CO_2 and drier Holocene and Eemian, did not yield the highest $\delta^{13}C$ values suggesting that these factors are not driving alkane $\delta^{13}C$ patterns.

Text S8. Downcore *n*-alkanoic acid δD and $\delta^{13}C$

In GLAD1-GSL00-4, downcore C_{28} and C_{30} alkanoic acid δD both ranged between approximately –220‰ and –170‰ (**Figure S18a**). For carbon isotopes, C_{28} and C_{30} alkanoic acid $\delta^{13}C$ averaged –26.3 ‰ (1σ = 2.3‰) and –27.6‰ (1σ = 2.0‰) (**Figure S18c**). In GLAD1-BL00-1, downcore C_{26}, C_{28}, and C_{30} alkanoic acid δD ranged between approximately –270‰ and –160‰, –230‰ and –160‰, and –230‰ and –160‰ (**Figure S18b**), while $\delta^{13}C$ averaged –30.3‰ (1σ = 2.4‰), –32.2‰ (1σ = 1.9‰), and –31.4‰ (1σ = 2.1‰) (**Figure S18d**). Bear Lake

$\delta^{13}C$ values were lower than those from Great Salt Lake by 4–6‰. We do not observe glacial-interglacial signals in either lake's *n*-alkanoic acid $\delta^{13}C$. We note low $\delta^{13}C$ values at Great Salt Lake preceding/during deep lake phases, although low values also occurred at other times. Great Salt Lake *n*-alkanoic acid $\delta^{13}C$ values are generally much higher than its *n*-alkane values as well as Bear Lake $\delta^{13}C$ from both compound classes, implying a different source.

Text S9. Consideration of alkyl lipid sourcing

Here, we discuss potential differences in the vegetational contributions of *n*-alkanes and *n*-alkanoic acids to the two lakes, using this information to determine the best compound to use for δD_{precip} reconstructions. Great Salt Lake and Bear Lake had comparable abundances of long-chain *n*-alkanes (averaging ~5–6 µg/gdw) and long-chain *n*-alkanoic acids (averaging ~30–50 µg/gdw) (**Figure S14**). Both had similar distributions in their alkyl lipids with the same modal chain lengths for both compound classes (C_{29} for *n*-alkanes, C_{26} for *n*-alkanoic acid) (**Figure S15**). As both lakes are part of the same catchment, similar lipid concentrations and distributions would be expected as they likely share some vegetational contributions. CPI is used as a sourcing metric with low values (i.e., ~1) characteristic of degradation/thermal maturity, or algal/microbial inputs, and high values (i.e., >4) of fresh terrestrial vegetation (Freeman and Pancost, 2014 and references therein). Regarding *n*-alkanes, the near unimodal lipid distributions, high downcore CPI (most >4), and measured $\delta^{13}C$ values in line with plants using the C_3 photosynthetic pathway suggests *n*-alkanes from both lakes are sourced primarily from terrestrial vegetation. As modern catchment plants also measure $\delta^{13}C$ values in line with C_3 plants, this downcore C_3 signal is expected. As downcore $\delta^{13}C$ for both compound classes did not show glacial-interglacial variability at either lake (**Figure S17c-d, S18c-d**), on the first order, $\delta^{13}C$ is unlikely to be controlled by global-scale climate trends. As atmospheric CO_2 $\delta^{13}C$ varied <0.6‰ over the last 160 ky (Eggleston et al., 2016), the majority of downcore lipid $\delta^{13}C$ variability is likely due to differential sourcing of these compounds.

It is notable that downcore $\delta^{13}C$ and δD values for samples with CPI <4 were not apparent outliers, with low CPI samples having isotope values in the same range as those of high CPI samples. However, regarding *n*-alkanoic acids, the downcore records were more complex. At Great Salt Lake in particular, while the *n*-alkanoic acids also had near unimodal lipid distributions and high CPI (**Figure S15c**), they had much higher $\delta^{13}C$ values (as high as –22‰) than what was seen in catchment plant *n*-alkanoic acid $\delta^{13}C$ (**Figure S18c**). These higher values suggest an input of *n*-alkanoic acids enriched in ^{13}C from a non-terrestrial plant source.

There seems to be greater shared vegetational contributions to the *n*-alkane pools at both lakes compared to *n*-alkanoic acid. The two lakes' downcore *n*-alkane records have the same range in $\delta^{13}C$ values (~–34‰ to –28‰) and a progressive depletion with increasing chain length (**Figure S17c-d**). For the same sample, the C_{27} alkane $\delta^{13}C$ tends to be 2–3‰ higher (though can be as much as 7‰ higher) than the C_{31} $\delta^{13}C$, with the C_{29} $\delta^{13}C$ having intermediate values between them. Such a trend of decreasing $\delta^{13}C$ with increasing chain length was also observed in modern catchment sediments (a ~3‰ difference between the mean C_{27} and C_{31} alkane $\delta^{13}C$; **Figure S9**) but was largely absent in catchment plants (**Figure S8**). Thus, the observed decline in $\delta^{13}C$ in both surface and downcore sediments with increasing chain length is likely due to inputs from sources other than the C_3 terrestrial vegetation. Specifically, increasing inputs of shorter chain length *n*-alkanes from sources enriched in ^{13}C.

The same patterns were not observed for the *n*-alkanoic acid records. *n*-Alkanoic acid $\delta^{13}C$ at Great Salt Lake was on average ~4‰ higher than at Bear Lake and recorded the highest values out of all $\delta^{13}C$ measurements (**Figure S18**). In modern catchment samples, measured $\delta^{13}C$

values were largely below 30‰ (**Figure S8**). The high values we see in Great Salt Lake *n*-alkanoic acid $\delta^{13}C$ is likely from a source enriched in ^{13}C other than the C_3 land plants. A possible source is contributions from submerged macrophytes, which have been found to produce long-chain *n*-alkanes with C_4-like $\delta^{13}C$ signatures (Aichner et al., 2010). While macrophytes are unlikely to be abundant at hypersaline Great Salt Lake, brackish conditions along the margin would allow for macrophyte productivity and the produced *n*-alkanoic acids can then be transported and deposited deeper in the lake.

Plant wax inputs are likely to be dominantly aeolian, with long range transport of plant wax possible (within a lake catchment; Nelson et al., 2017) (across an ocean basin; Conte and Weber, 2002). Great Salt Lake has 15 times the surface area, with less surrounding vegetation and lower relief, than Bear Lake. This may imply a greater contribution of long-range aerial deposition at Great Salt Lake. Whereas Bear Lake is likely dominated by local wind-blown inputs. Given the sites' high elevations, C4 plants are unlikely to contribute to either record. Conte and Weber (2002) found that aerosol samples collected from Bermuda had about twice as much *n*-alkanoic acids than *n*-alkanes. Assuming aerosols deposited at Great Salt Lake similarly had greater proportional abundances of *n*-alkanoic acids, this would still be insufficient to explain the enriched downcore *n*-alkanoic acid $\delta^{13}C$ signal given that Great Salt Lake *n*-alkanes are not enriched compared to Bear Lake *n*-alkanes. Further, downcore Great Salt Lake *n*-alkanoic acids are ~7–8 times more abundant than *n*-alkanes (**Figure S14a**), so aerosol *n*-alkanoic acids would have to be significantly more abundant than their *n*-alkane counterparts in order to yield an enriched downcore $\delta^{13}C$ signal. Thus, it is unlikely for aeolian-transport of aerosolized waxes to be the cause of enriched *n*-alkanoic acid $\delta^{13}C$ at Great Salt Lake.

As vegetation inputs to both lakes are dominantly C_3, $\delta^{13}C$ values are not expected to be higher than –30‰ from plants, with values higher than –30‰ likely including aquatic contributions. Downcore *n*-alkanoic acid $\delta^{13}C$ values were frequently >–30‰ at Great Salt Lake (**Figure S17c-d, S18c-d**), indicating significant aquatic contributions of *n*-alkanoic acids. *n*-Alkane $\delta^{13}C$ at both lakes, are largely below –30‰, but increasing $\delta^{13}C$ values with decreasing chain length suggests increasing contributions from aquatic or microbial sources. As the C_{31} alkane $\delta^{13}C$ stayed below –30‰ consistently at Bear Lake and most frequently at Great Salt Lake, we infer the C_{31} alkane receives the least aquatic additions and thus is selected for precipitation δD (δD_{precip}) reconstructions.

Text S10. Pollen-adjusted downcore $\varepsilon_{wax/water}$

Here, we consider possible changes in $\varepsilon_{wax/water}$ due to shifts in vegetation composition. For all plant samples with measurable C_{31} alkane quantities (n = 17), the C_{31} alkane abundance weighted average δD is –214‰. For an annual δD_{precip} of –112‰ at Bear Lake (Waterisotopes Database, 2025a), the calculated $\varepsilon_{wax/water}$ is –115‰. However, as regional plants likely utilize winter precipitation, a Nov-Apr δD_{precip} of –141‰ (weighted based on liquid precipitation amounts per month) would yield an $\varepsilon_{wax/water}$ of –85‰. The three plant groups producing the majority of C_{31} alkanes are *Artemisia tridentata* (55%), asters (33%), and graminoids (6%) (**Figure S5**). The average C_{31} alkane δD for the three groups are –209±23‰, –231±7‰, and –284±12‰ (**Figure S10**). Based on this, changes in the proportion of graminoids are the most likely to change $\varepsilon_{wax/water}$. We use the downcore GLAD1-BL00-1 pollen abundances of these three groups (which make up approximately 40–70% of all pollen) along with the Nov-Apr δD_{precip} of –141‰ to estimate downcore changes in $\varepsilon_{wax/water}$. We found the pollen-weighted average $\varepsilon_{wax/water}$ to be –93±6‰ (full range being –119 to –83‰), similar to the $\varepsilon_{wax/water}$ determined by Feakins and Sessions (2010) and used for our δD_{precip} calculations. Allowing

$\varepsilon_{wax/water}$ to vary downcore based on pollen abundances does not change the broad glacial-interglacial trends in calculated δD_{precip}.

Text S11. Snow proportion system of equations for δD_{precip} calculations

Changes in the proportion of precipitation falling as snow, specifically in terms of snow water equivalent, as opposed to rain changes δD_{precip} due to snow's greater degree of D-depletion. For each lake, we set up a simple linear equation to calculate δD_{precip} based on snow proportion:

$$\delta D_{precip} = m \times p_{snow} + b$$

where: p_{snow} = snow proportion, δD_{precip} = δD of precipitation at lake sites, and m and b are the unknown slope and y-intercept.

We solve for m and b using known values of δD_{precip} and p_{snow}. We take the present-day δD_{precip} of the lakes (Great Salt Lake = –103 ± 2‰, Bear Lake = –112 ± 1‰) along with their present-day snow proportions (20% and 30%) then extrapolate to 100% of precipitation being snowfall, assuming the δD_{precip} would then be equivalent to δD_{snow} (–148 ± 15‰) (Waterisotopes Database, 2017a, b, c, d). Based on this information, the systems of equations for the two lakes are the following:

Great Salt Lake: $-103‰ = m \times 0.2 + b$ $\quad -148‰ = m \times 1 + b$

Bear Lake: $-112‰ = m \times 0.3 + b$ $\quad -148‰ = m \times 1 + b$

Solving these systems of equations, we determined the slope m to be –0.56 for Great Salt Lake and –0.51 for Bear Lake. Thus, for every 10% increase in the proportion of snow, δD_{precip} will decrease by about 5.6‰ at Great Salt Lake and by 5.1‰ at Bear Lake.

Text S12. Moisture source mixing model equations for δD_{precip} calculations

Modern precitipiation in Utah is dominated by winter season precipitation (**Figure 2**) with δD values and storm tracks indicating the dominance of Pacific sources (Friedman et al., 2002). We set up a simple mixing model to estimate the proportion of precipitation from northerly and southerly storms:

$$\delta D_{precip} = p_{north} \times \delta D_{north} + p_{tropical} \times \delta D_{tropical}$$

$$1 = p_{north} + p_{tropical}$$

where: p_{north} = proportion of North Pacific storms, $p_{tropical}$ = proportion of tropical Pacific storms, δD_{north} = precipitation δD of North Pacific storms = –112 ± 37‰, $\delta D_{tropical}$ = precipitation δD of tropical Pacific storms = –81 ± 37‰, δD_{precip} = δD of precipitation at lake sites.

An increase in the proportion of North Pacific storms will result in a δD_{precip} closer to –112‰ while an increase in tropical Pacific storms results in a value closer to –81‰. Under this scenario, each 10% increase in the proportion of North Pacific storms causes δD_{precip} to decrease by ~3‰. A more extreme scenario occurs if we use a higher δD_{precip} for tropical Pacific storms (plus 1σ value of –44‰) and a lower δD_{precip} for North Pacific storms (minus 1σ value of –149‰), which results in a δD_{precip} change of ~10‰ for each 10% change in storm proportions. We do not attempt calculations with a lower tropical Pacific δD_{precip} and higher North Pacific

δD_{precip} values as that would cause the latter to have higher values than the former, an unlikely scenario given latitudinal relations in precipitation isotopes. Given Nov-Apr δD_{precip} at present-day Salt Lake City is –120‰ (1σ = 31‰) (Waterisotopes Database, 2024), we expect a scenario somewhere between the average and more extreme scenarios to be driving δD_{precip} at our lake sites.

Supplementary Figures

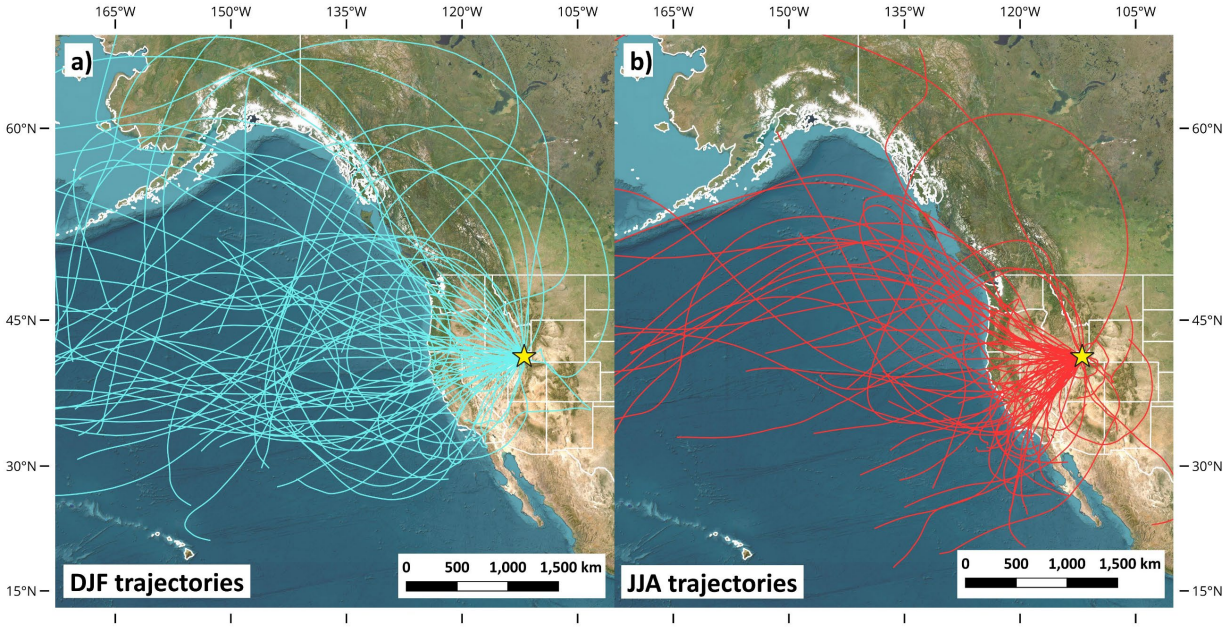

Figure S1. Map of NOAA HYSPLIT4 air mass at ~500 hPa back trajectories for a) December, January, and February (DJF), and b) June, July, and August (JJA) (Rolph et al., 2017; Stein et al., 2015). The origin of the trajectories (yellow star) is halfway between Great Salt Lake and Bear Lake. Trajectories are from NOAA archives for Dec 2019–Aug 2024.

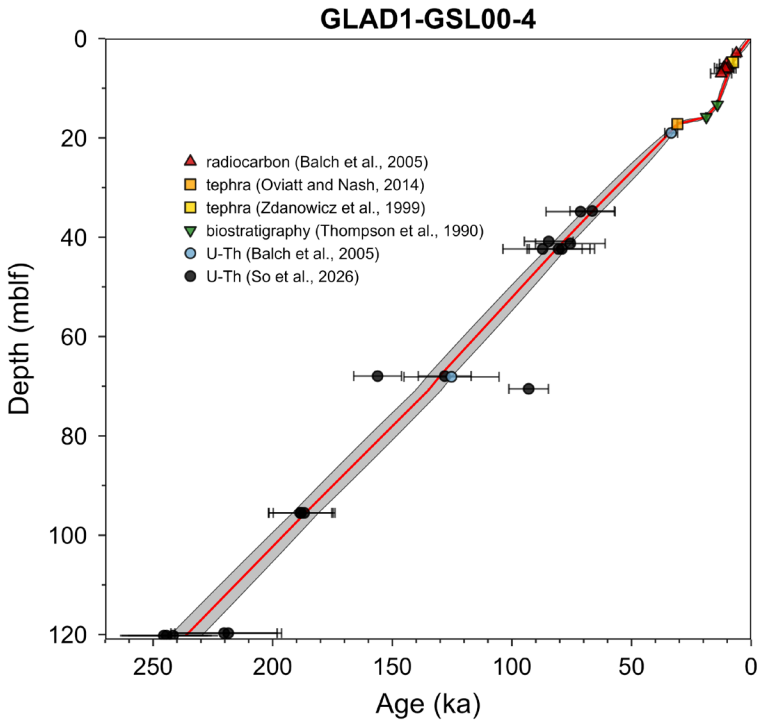

Figure S2. Age model for the GLAD1-GSL00-4 sediment core showing the average age (red line) and the 2σ age envelope (gray). Error bars represent 2σ age uncertainty for each data point. Age model reproduced from So et al. (2026).

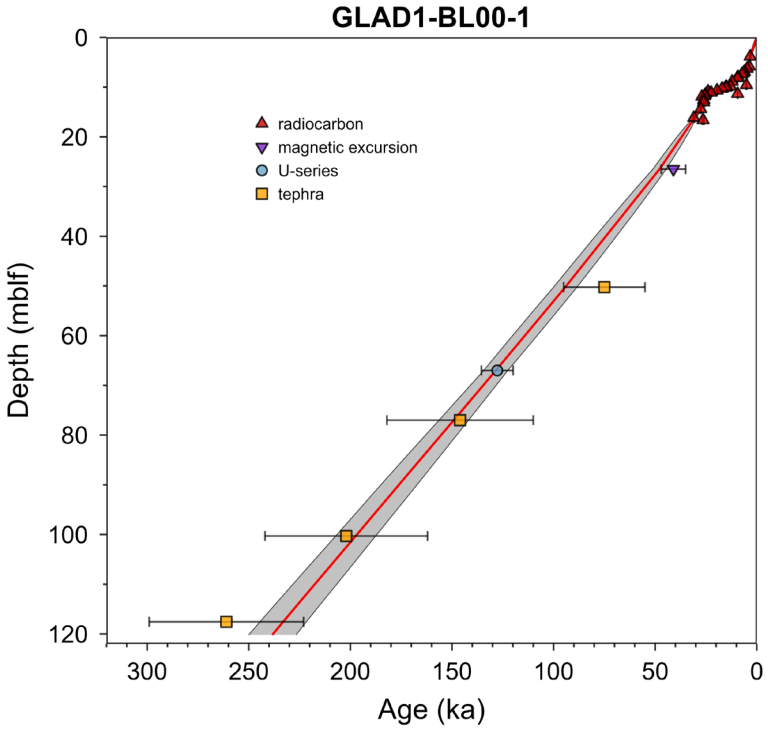

Figure S3. Age model for GLAD1-BL00-1 sediment core showing the average age (red line) and the 2σ age envelope (gray). Error bars represent 2σ age uncertainty for each data point. All data used for age model development is from Colman et al. (2006).

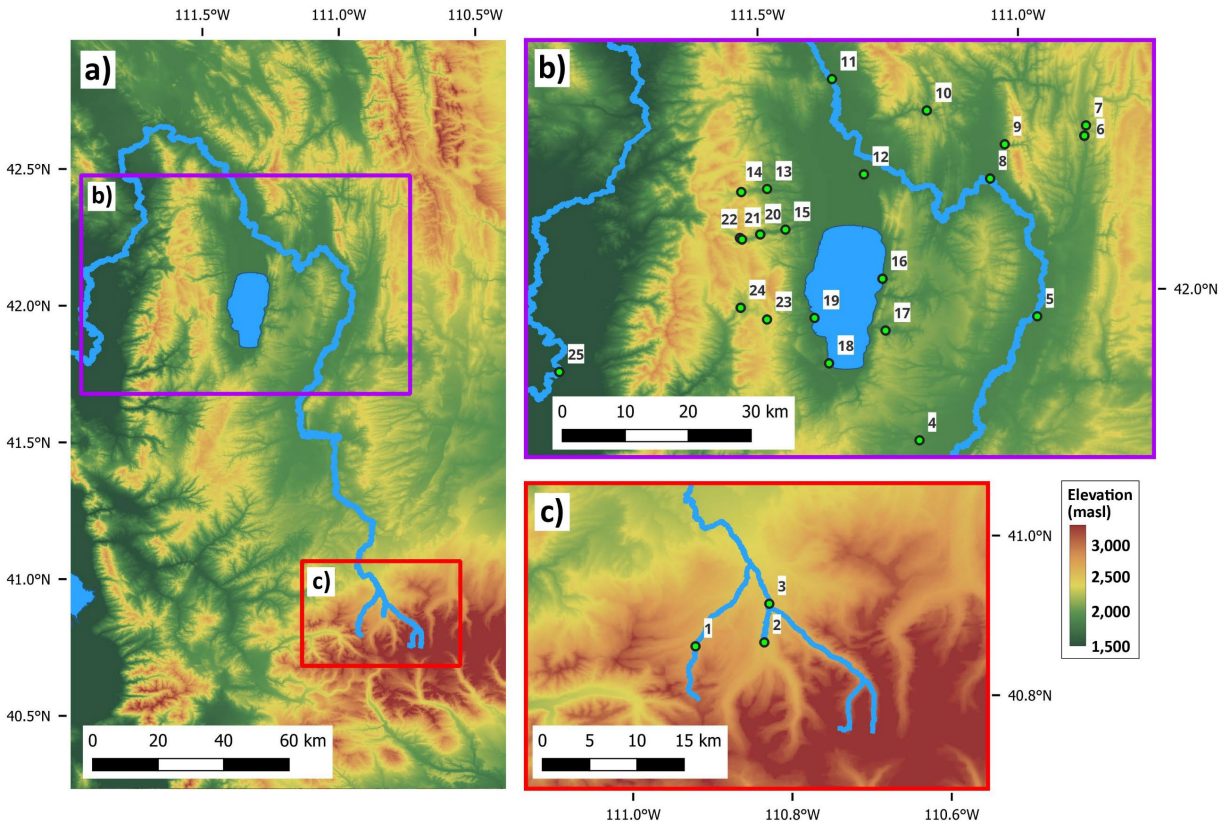

Figure S4. Map of the Bear Lake catchment (a) showing modern sampling sites around Bear Lake (b) and at the headwaters of the Bear River in the Uinta Mountains (c). Information on each sample is shown in Table S1.

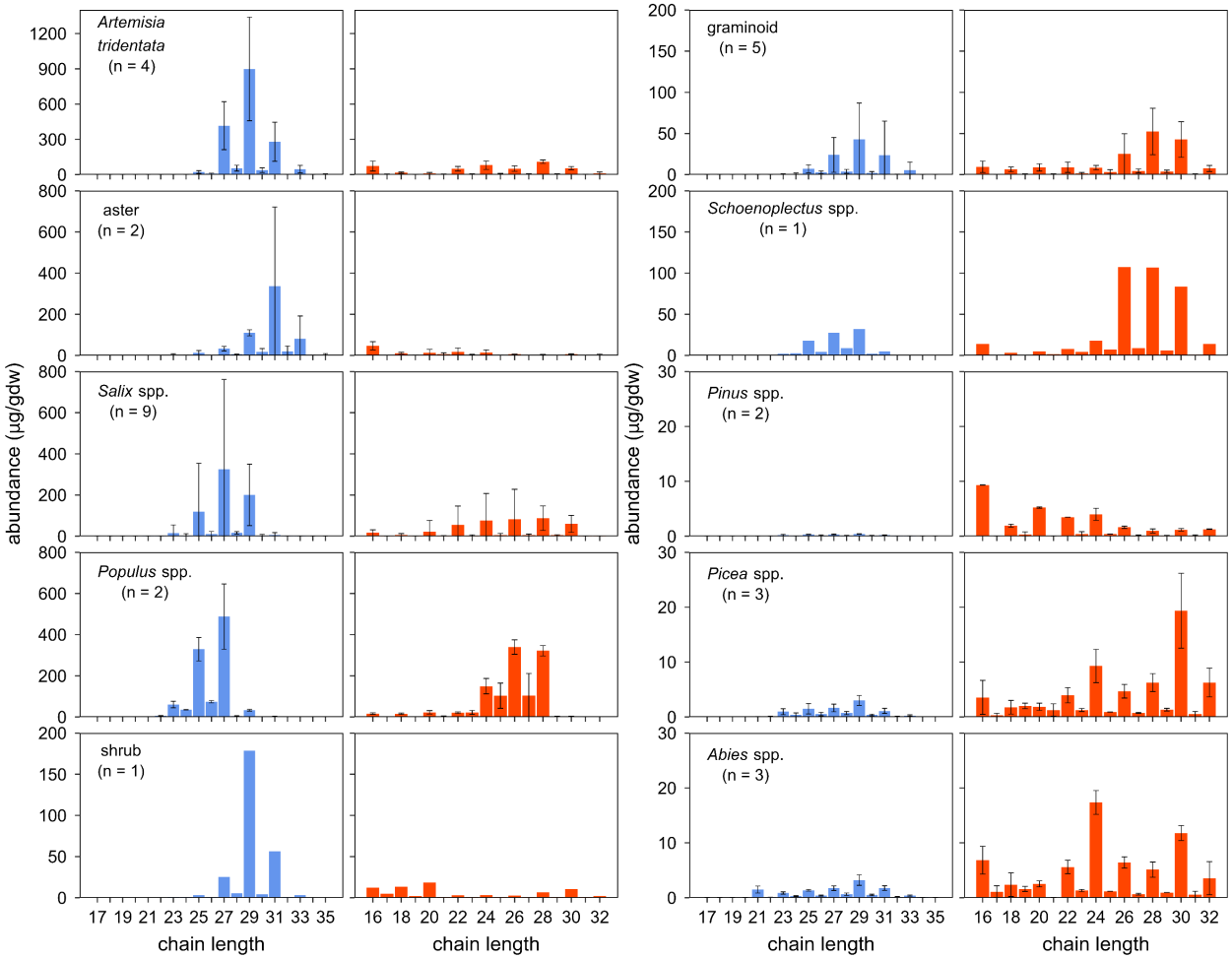

Figure S5. Absolute abundances of *n*-alkanes (blue) and *n*-alkanoic acids (orange) by chain length for modern plants in the Bear Lake catchment, broadly grouped by species, genus, or growth form. Plant groups are ordered from highest to lowest wax abundance going left to right, and top down. Error bars represent 1σ from the mean for plant groups with more than one sample.

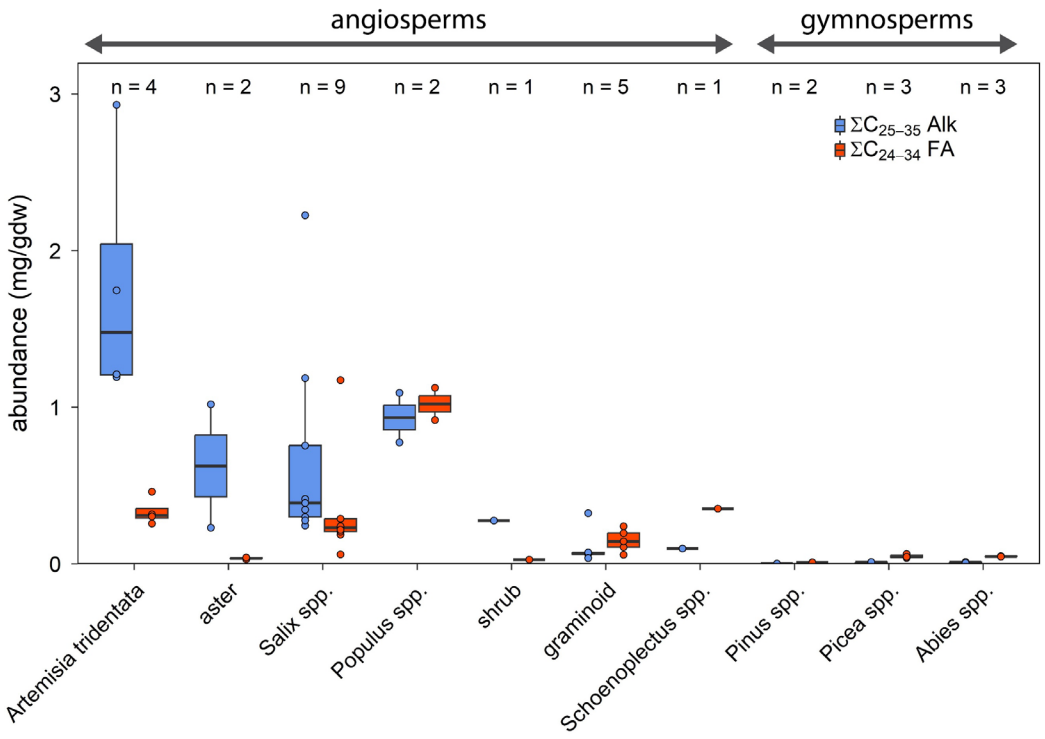

Figure S6. Absolute abundances of long-chain *n*-alkanes (C_{25}-C_{35}; blue) and long-chain *n*-alkanoic acids (C_{24}-C_{34}; orange) for modern plants in the Bear Lake catchment, broadly grouped by species, genus, or growth form. Plant groups are ordered from highest to lowest wax abundance going left to right. Error bars represent 1σ from the mean for plant groups with more than one sample.

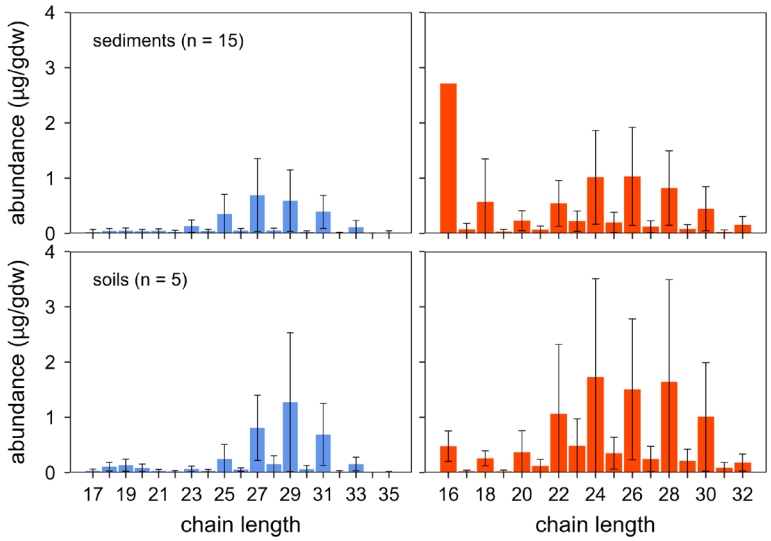

Figure S7. Absolute abundances of *n*-alkanes (blue) and *n*-alkanoic acids (orange) by chain length for modern sediments (top) and soils (bottom) in the Bear Lake catchment. Sediments were collected from Bear Lake and connected streams. Soils were collected adjacent to select sediment collection sites. Error bars represent 1σ from the mean.

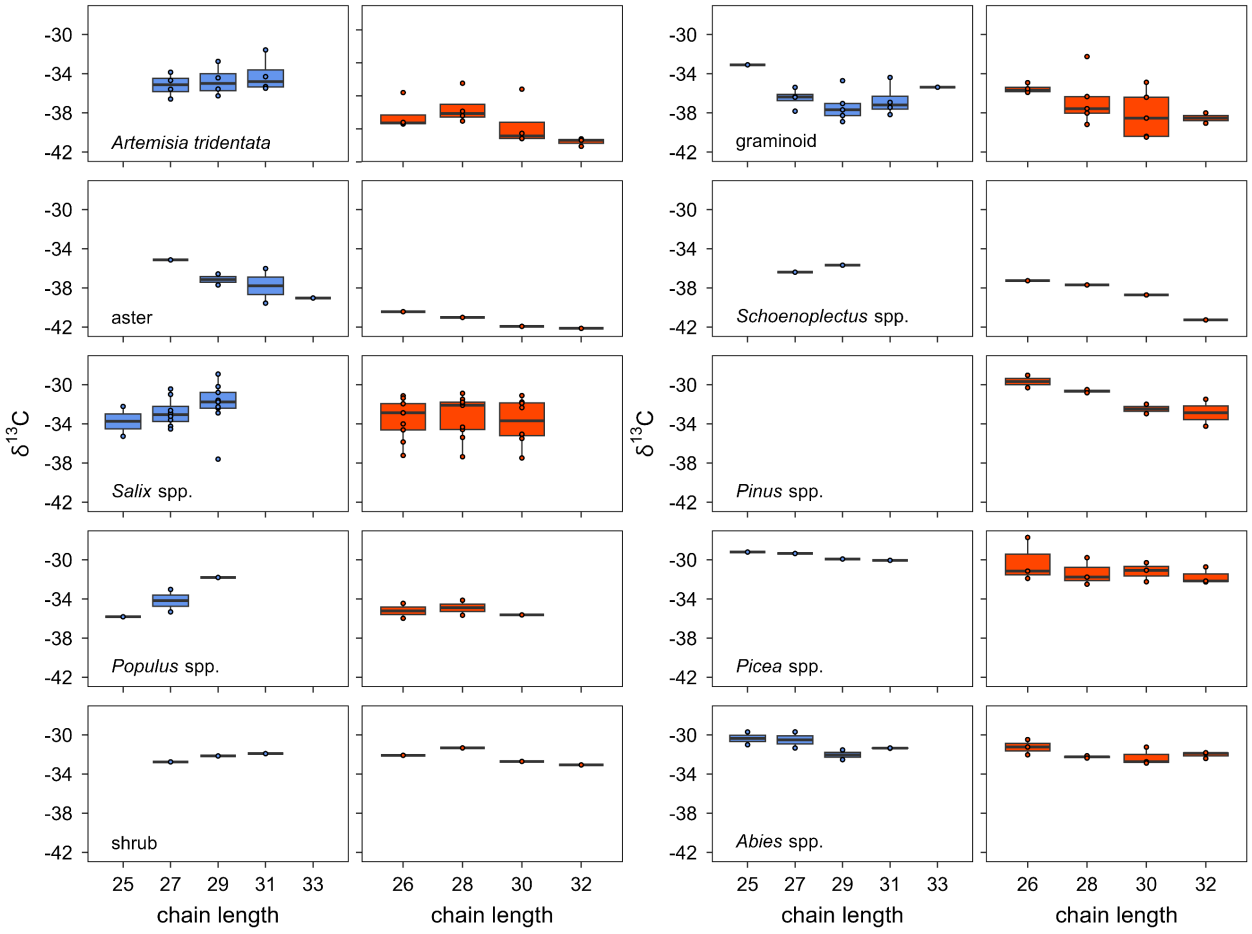

Figure S8. δ^{13}C of *n*-alkanes (blue) and *n*-alkanoic acids (orange) for modern plants in the Bear Lake catchment, broadly grouped by species, genus, or growth form. Plant groups are ordered from highest to lowest wax abundance going left to right, and top down. Empty plots indicate no δ^{13}C measurements were made.

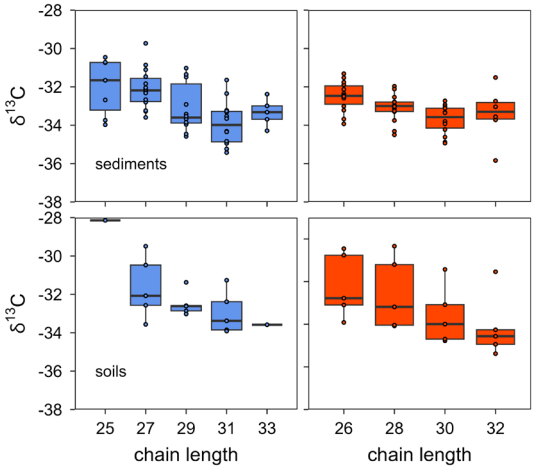

Figure S9. δ^{13}C of *n*-alkanes (blue) and *n*-alkanoic acids (orange) for modern sediments (top) and soils (bottom) in the Bear Lake catchment. Sediments were collected from Bear Lake and connected streams. Soils were collected adjacent to select sediment collection sites.

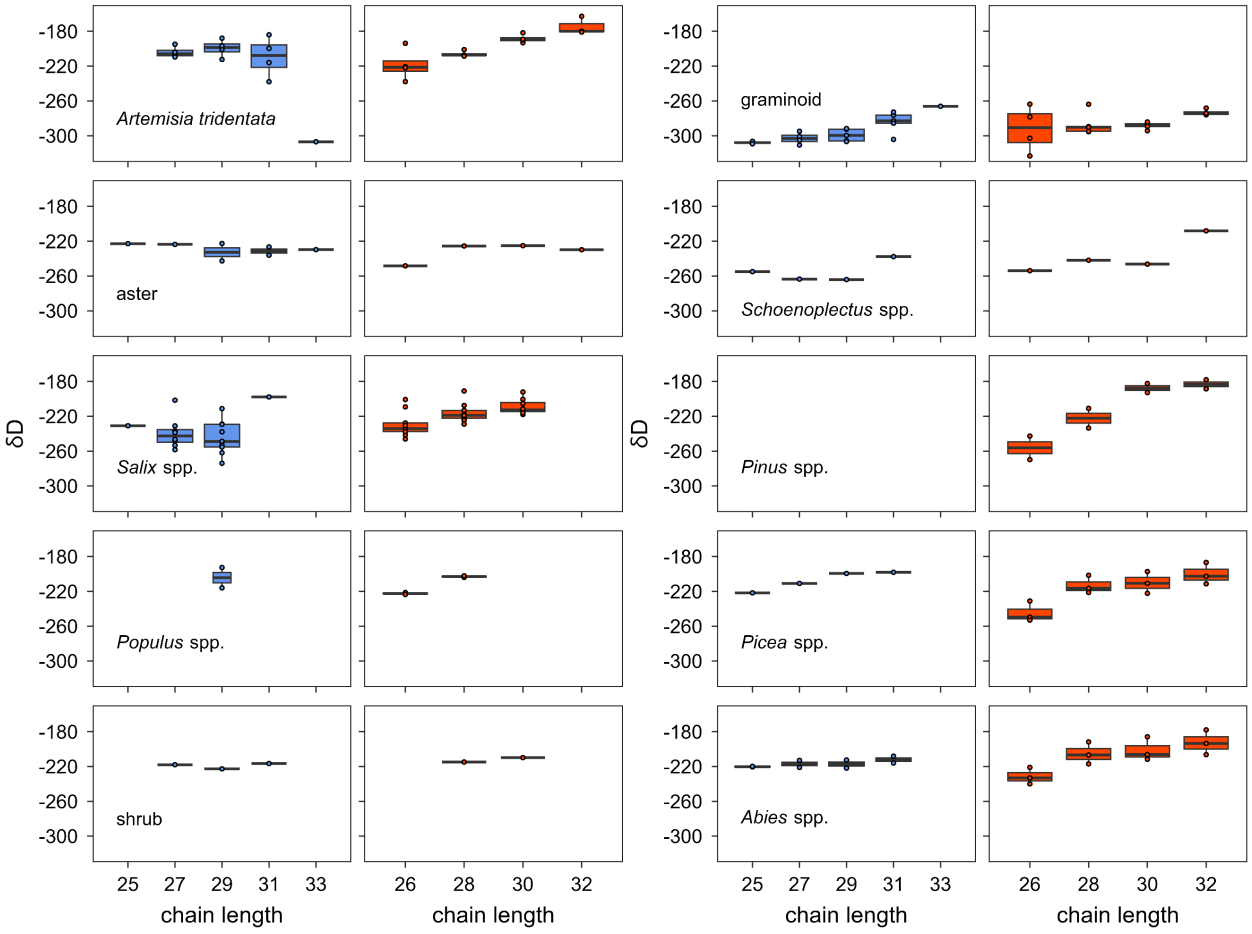

Figure S10. δD of *n*-alkanes (blue) and *n*-alkanoic acids (orange) for modern plants in the Bear Lake catchment, broadly grouped by species, genus, or growth form. Plant groups are ordered from highest to lowest wax abundance going left to right, and top down. Empty plots indicate no δD measurements were made.

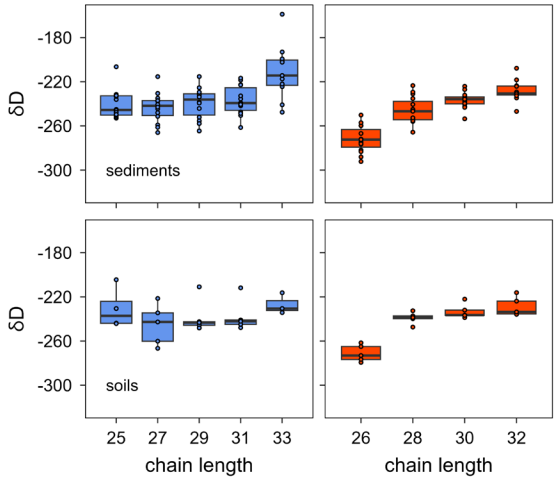

Figure S11. δD of *n*-alkanes (blue) and *n*-alkanoic acids (orange) for modern sediments (top) and soils (bottom) in the Bear Lake catchment. Sediments were collected from Bear Lake and connected streams. Soils were collected adjacent to select sediment collection sites.

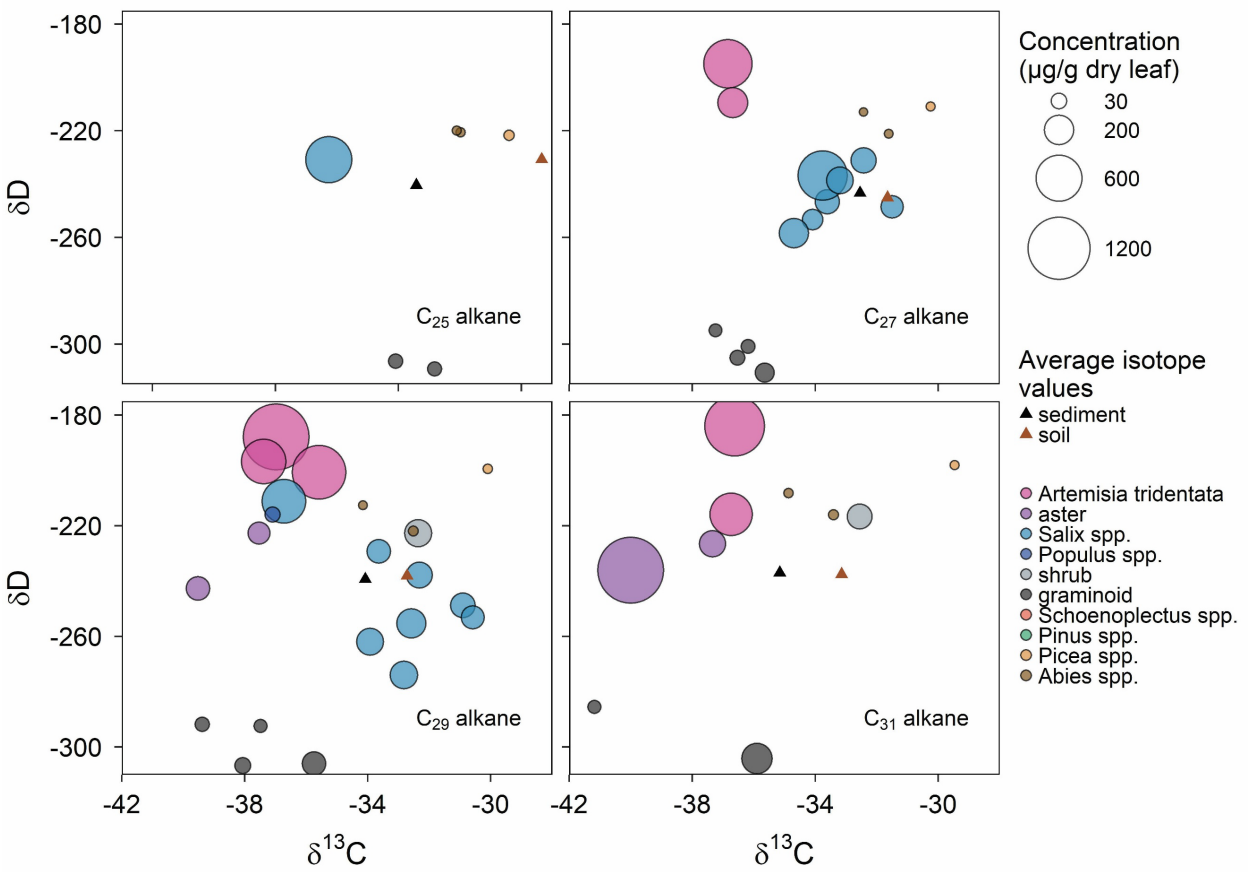

Figure S12. Cross plots of $\delta^{13}C$ and δD of individual plant samples for the C_{25}, C_{27}, C_{29}, and C_{31} alkanes. Circles represent individual plant samples with size indicating alkane concentrations, and colors indicating plant group. Average sediment and soil $\delta^{13}C$ and δD values are indicated in triangles (black and brown respectively).

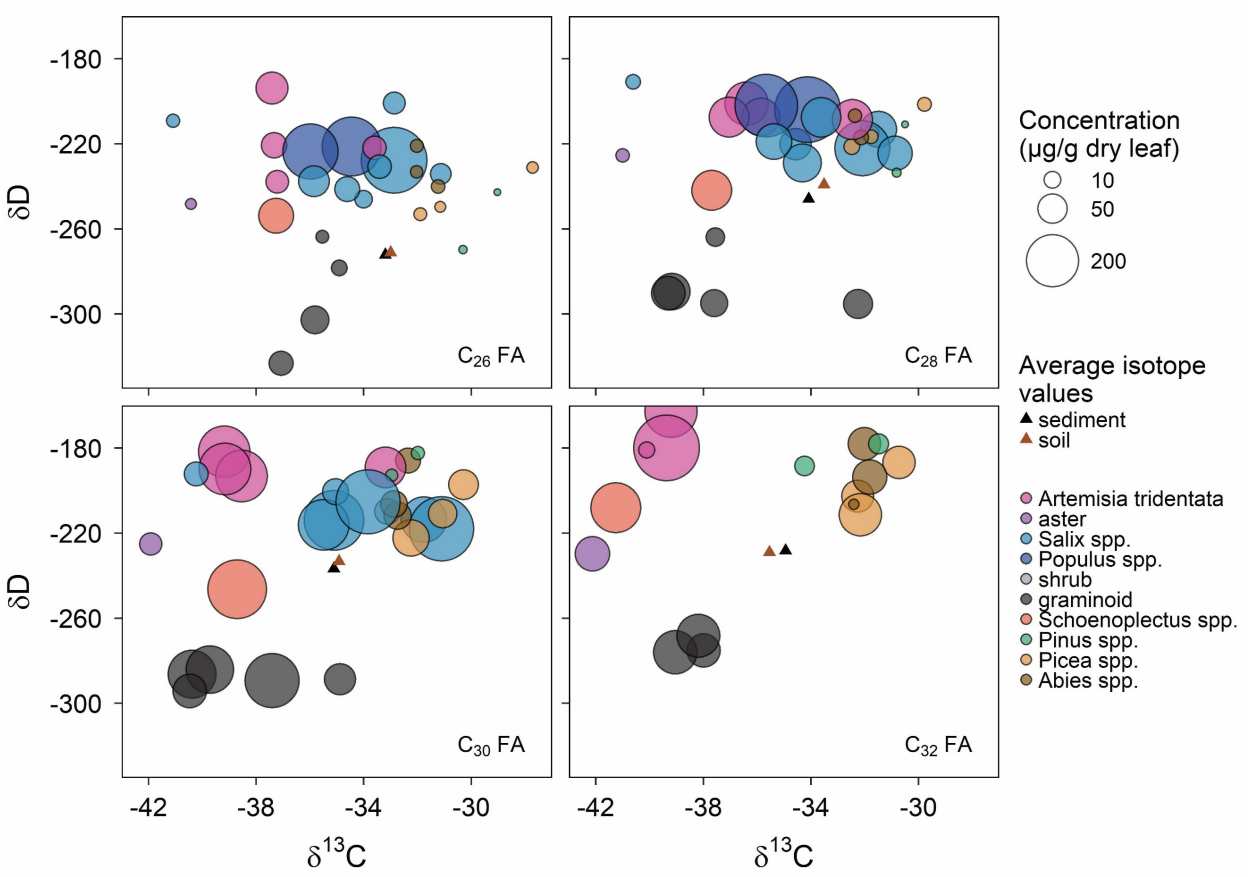

Figure S13. Cross plots of $\delta^{13}C$ and δD of individual plant samples for the C_{26}, C_{28}, C_{30}, and C_{32} alkanoic acids. Circles represent individual plant samples with size indicating alkanoic acid concentrations, and colors indicating plant group. Average sediment and soil $\delta^{13}C$ and δD values are indicated in triangles (black and brown respectively).

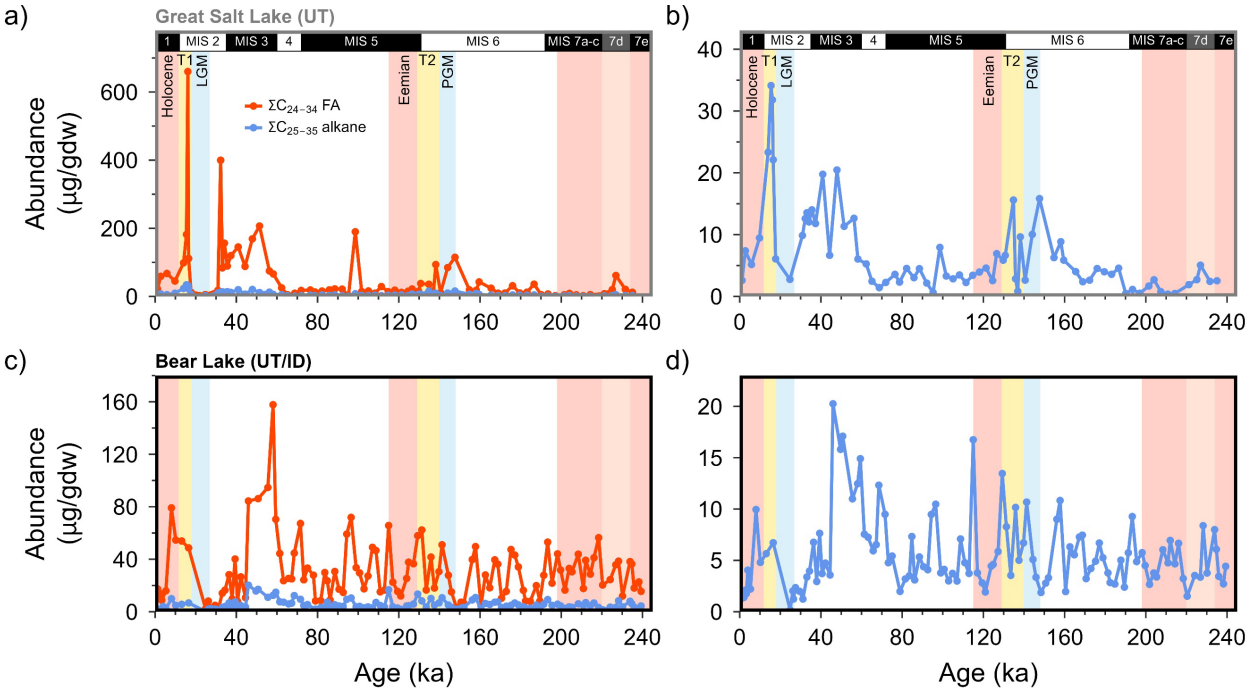

Figure S14. Downcore abundances for a, b) long-chain *n*-alkanes (blue) and long-chain *n*-alkanoic acids (orange) in GLAD1-GSL00-4 (gray border), and c, d) long-chain *n*-alkanes (blue) and long-chain *n*-alkanoic acids (orange) in GLAD1-BL00-1 (black border). Pink color-shaded boxes indicate interglacial intervals, yellow boxes are glacial terminations, and blue boxes are glacial maxima. b) and d) show individual *n*-alkane abundances on a differently scaled y-axis.

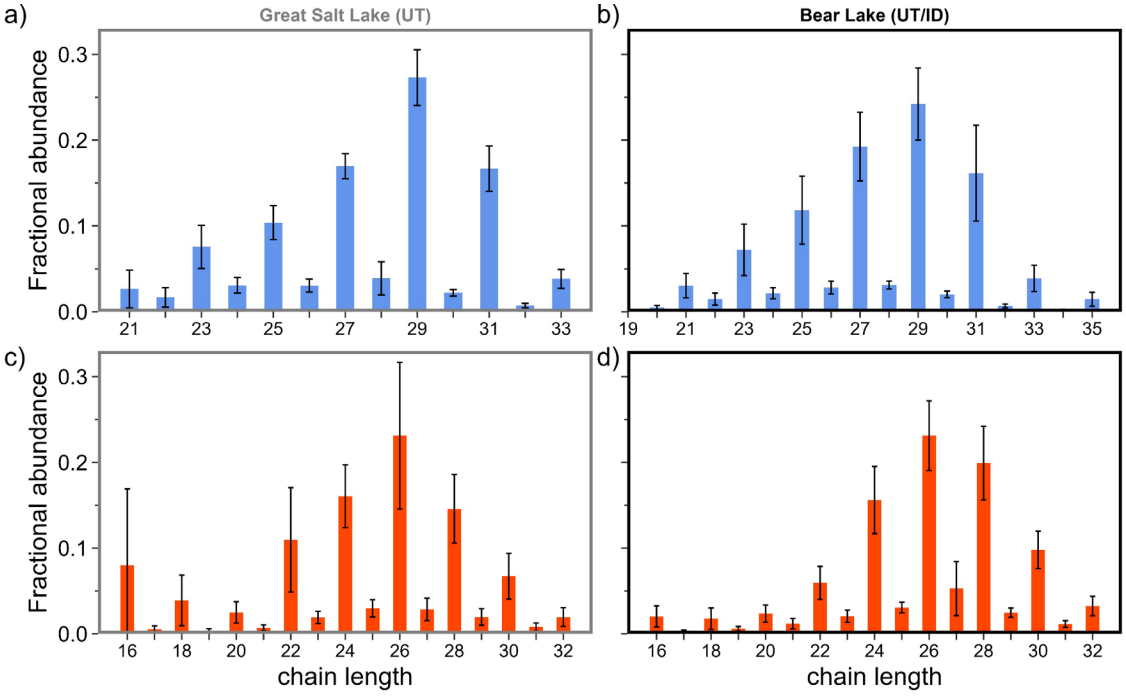

Figure S15. Average fractional abundances of *n*-alkanes (top) and *n*-alkanoic acids (bottom) by chain length for all samples in a,c) GLAD1-GSL00-4 (gray border), and b,d) GLAD1-BL00-1 (black border).

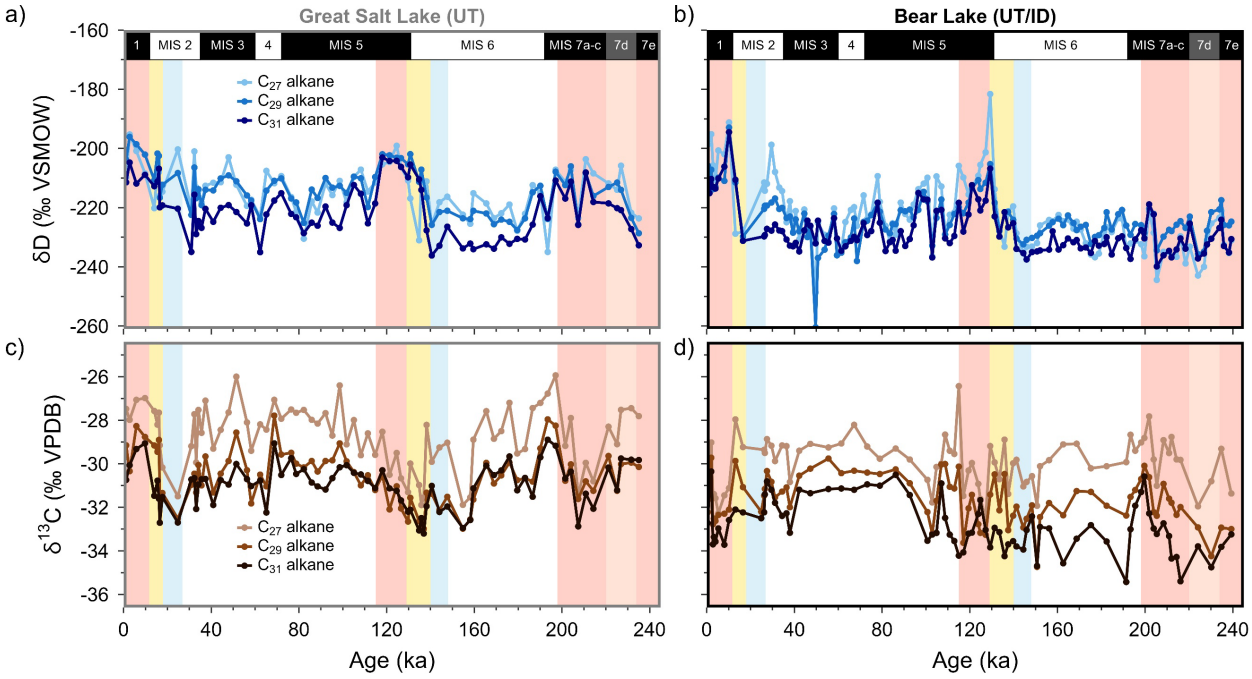

Figure S16. δD (blue) and $\delta^{13}C$ (brown) values for C_{27}, C_{29}, and C_{31} alkanes downcore for a,c) GLAD1-GSL00-4 (gray border) and b,d) GLAD1-BL00-1 (black border). Pink color-shaded boxes indicate interglacial intervals, yellow boxes are glacial terminations, and blue boxes are glacial maxima.

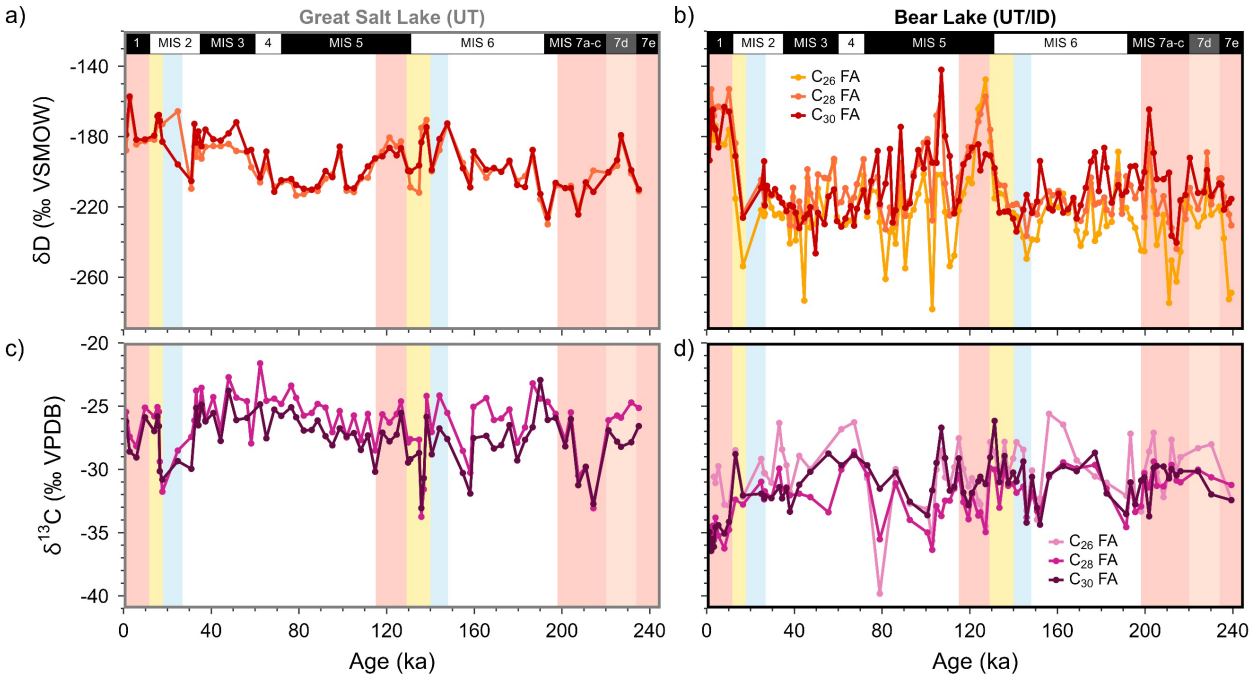

Figure S17. δD (orange) and δ13C (pink) values for C_{26}, C_{28}, and C_{30} *n*-alkanoic acids for a,c) GLAD1-GSL00-4 (gray border) and b,d) GLAD BL00-1 (black border). Pink color-shaded boxes indicate interglacial intervals, yellow boxes are glacial terminations, and blue boxes are glacial maxima.

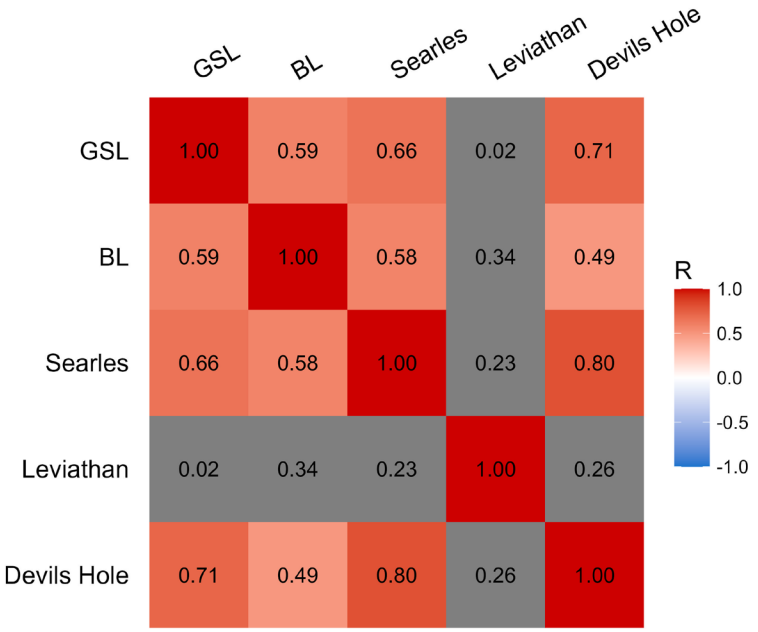

Figure S18. Correlation matrix showing R values of regional precipitation isotope records. Statistically insignificant values (p >0.05) are colored gray. GSL and BL stand for Great Salt Lake and Bear Lake respectively.

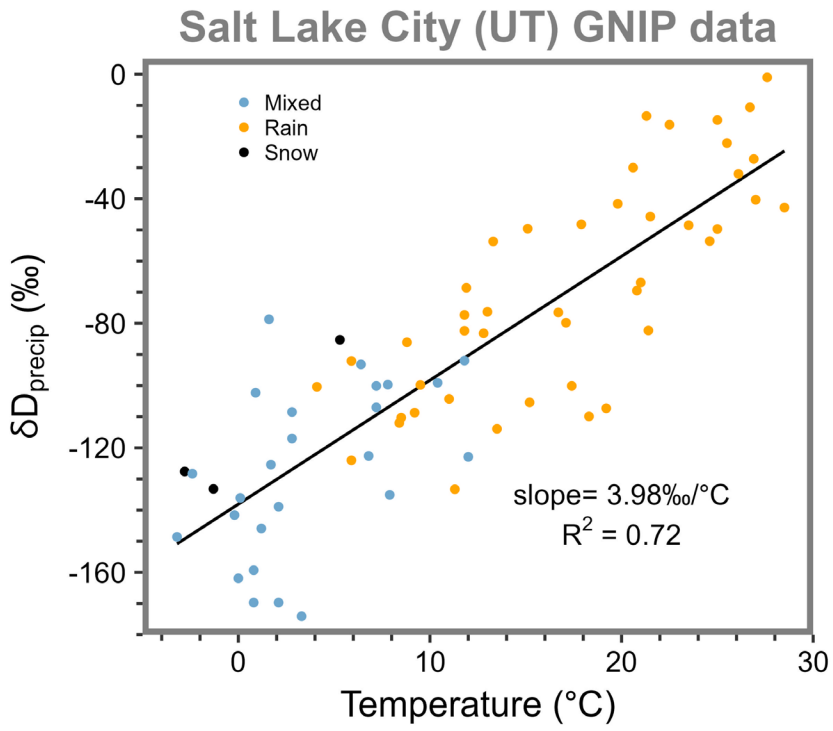

Figure S19. Salt Lake City precipitation δD plotted against temperature for the years 2015-2022, colored by precipitation type (Global Network of Isotopes in Precipitation, 2022).

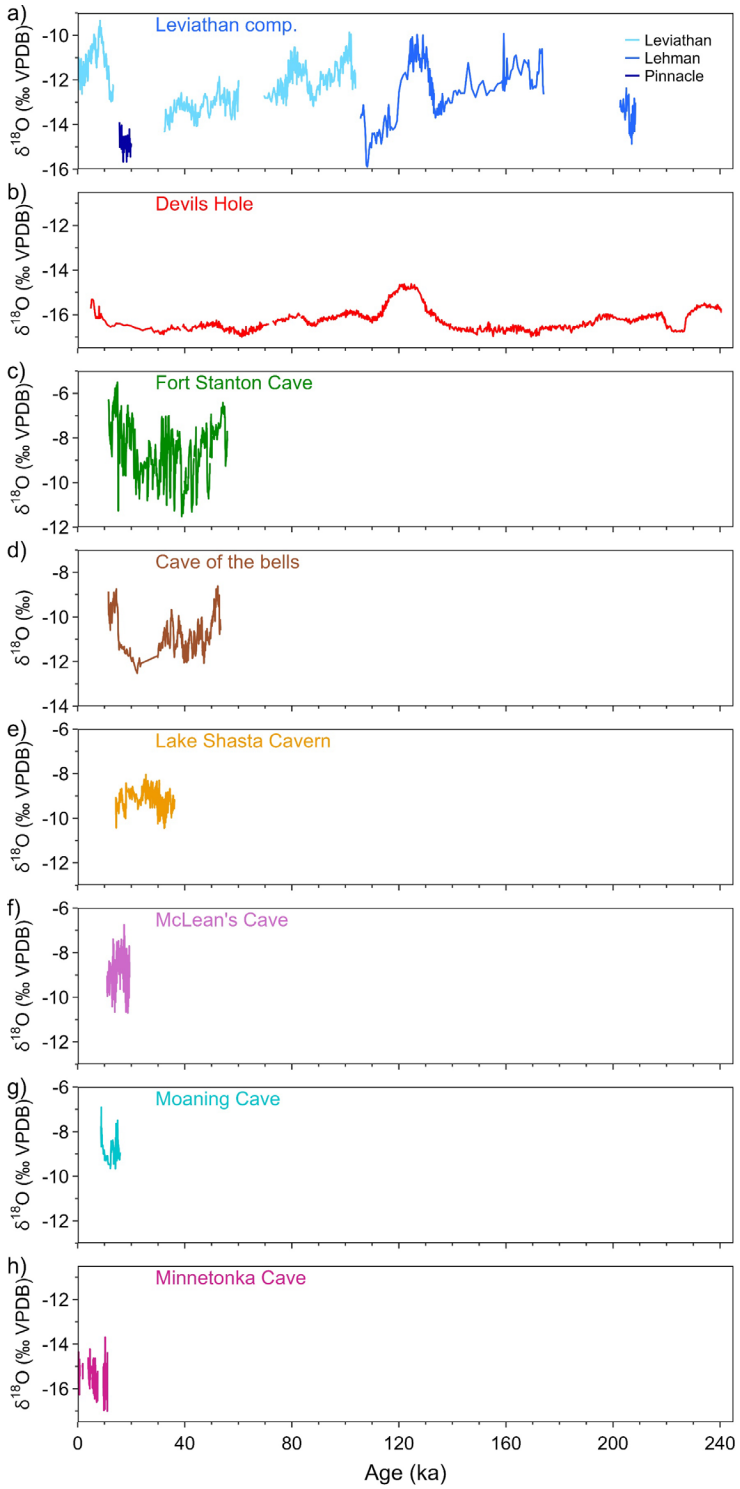

Figure S20. Comparison of speleothem $\delta^{18}O$ timeseries from a) Leviathan, Lehman, and Pinnacle Cave composite (Lachniet, 2016), b) Devils Hole at different depths within the cave (Wendt et al., 2025), c) Fort Stanton Cave (Asmerom et al., 2010), d) Cave of the Bells (Wagner et al., 2010), e) Lake Shasta Cavern (Oster et al., 2020), f) McLean's Cave (Oster et al., 2015), g) Moaning Cave (Oster et al., 2015), and h) Minnetonka Cave (UT) (Lundeen et al., 2013).

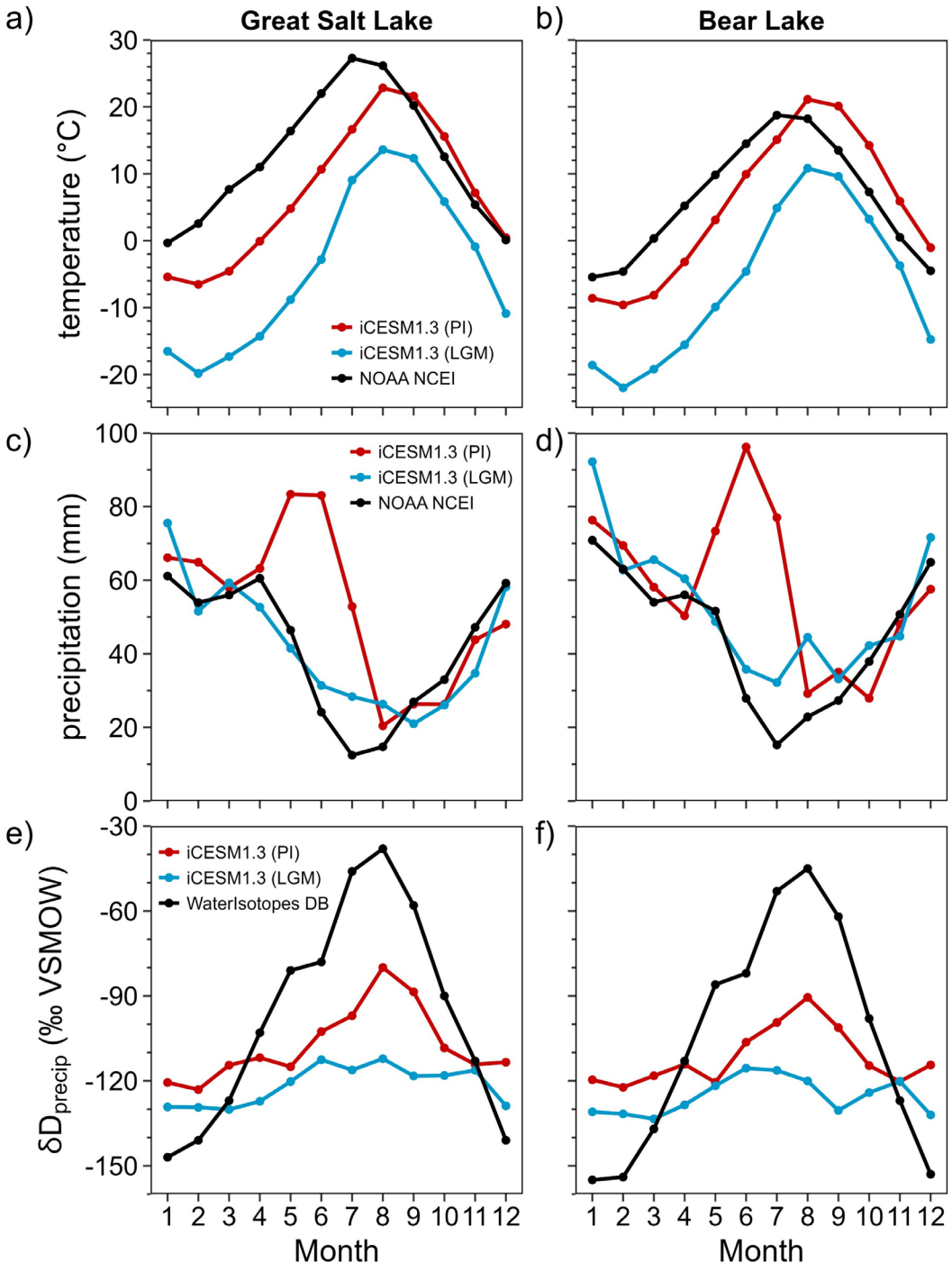

Figure S21. iCESM1.3 monthly output for pre-industrial (PI) and Last Glacial Maximum (LGM) compared to modern observations for a,b) temperature, c,d) precipitation amounts, and e,f) δD_{precip} at Great Salt Lake and Bear Lake. Modern temperature and precipitation are for Salt Lake City, UT (a,c), and Laketown, UT (b,d), from National Centers for Environmental Information (2020a, 2020b), data for the years 1991-2020. Modern δD_{precip} are from Waterisotopes Database (2025a, 2025b).

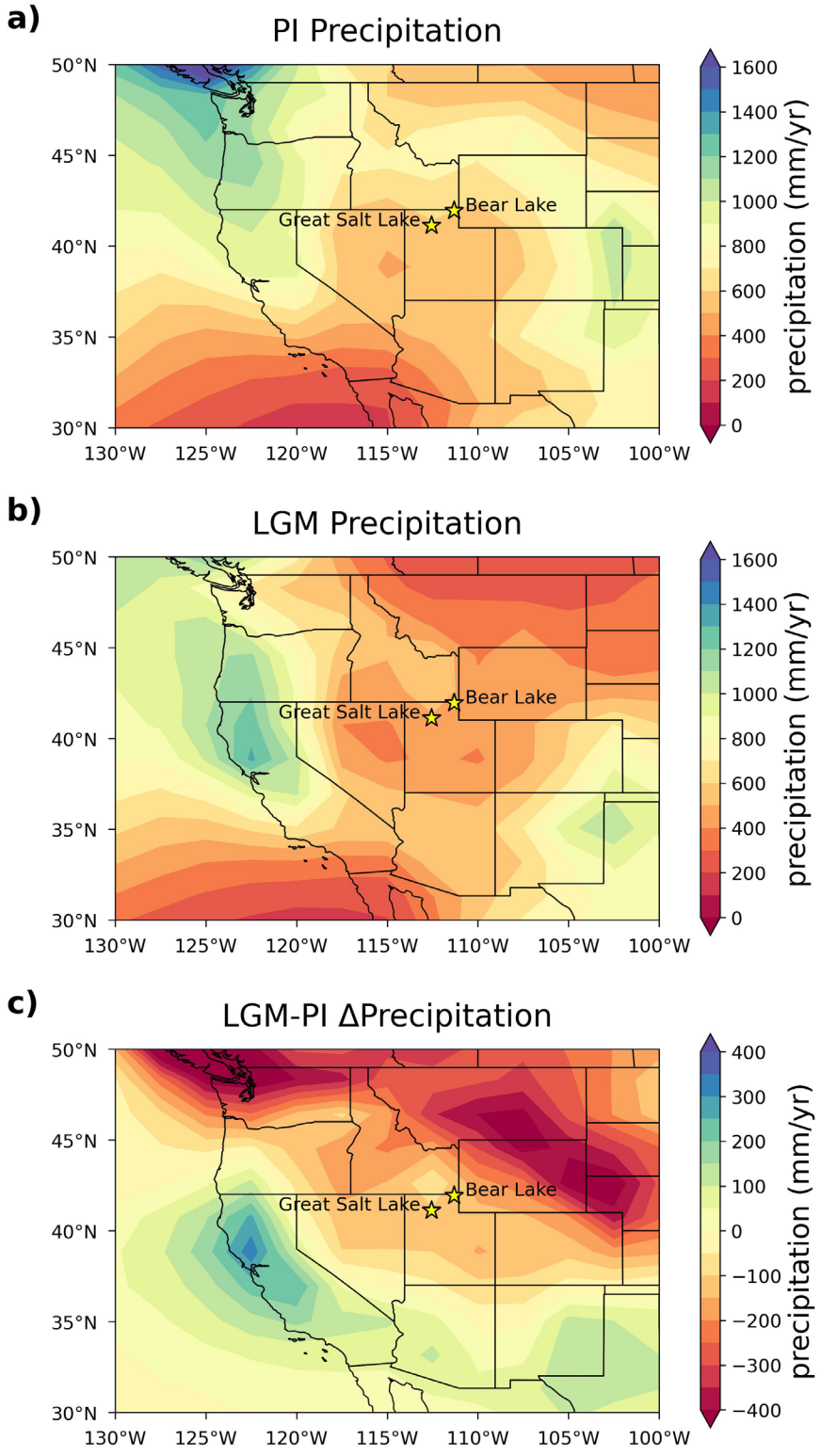

Figure S22. iCESM1.3 simulated annual precipitation amount for the a) pre-industrial (PI), b) Last Glacial Maximum (LGM), and c) difference between LGM and PI. The locations of Great Salt Lake and Bear Lake are indicated (yellow stars).

Table S1. List of sampling sites for plant, soil, and sediment samples in the modern Bear Lake catchment.

Site number	Sample ID	Sample type	Plant label	Plant family	Plant genus	Latitude	Longitude	Elevation (masl)
1	UI-01-Se	river sediment				40.8613	-110.9218	2713
2	UI-02-Se	river sediment				40.8662	-110.8354	2594
3	UI-03-Se	river sediment				40.9146	-110.8291	2519
4	BR-18-Se	river sediment				41.7099	-111.189	1924
5	BR-19-Se	river sediment				41.9474	-110.9631	1885
6	BR-01-Se	river sediment				42.2932	-110.8726	2071
6	BR-01-So	soil				42.2932	-110.8726	2071
6	BR-01-P1	plant	grass	*Poaceae*		42.2932	-110.8726	2071
6	BR-01-P2	plant	willow	*Salicaceae*	*Salix*	42.2932	-110.8726	2071
6	BR-01-P3	plant	shrub			42.2932	-110.8726	2071
7	BR-02-P	plant	Artemisia	*Asteraceae*	*Artemisia*	42.313	-110.8695	2087
8	BR-03-Se	river sediment				42.2112	-111.0535	1847
8	BR-03-So	soil				42.2112	-111.0535	1847
8	BR-03-P	plant	grass	*Poaceae*		42.2112	-111.0535	1847
9	BR-04-P	plant	Artemisia	*Asteraceae*	*Artemisia*	42.2768	-111.0255	1934
10	BR-05-P1	plant	Artemisia	*Asteraceae*	*Artemisia*	42.3415	-111.1751	1967
10	BR-05-P2	plant	willow	*Salicaceae*	*Salix*	42.3415	-111.1751	1967
10	BR-05-P3	plant	willow	*Salicaceae*	*Salix*	42.3415	-111.1751	1967
11	BR-06-Se	river sediment				42.4017	-111.3571	1816
11	BR-06-P1	plant	grass	*Poaceae*		42.4017	-111.3571	1816
11	BR-06-P2	plant	willow	*Salicaceae*	*Salix*	42.4017	-111.3571	1816
12	BR-07-Se	river sediment				42.2193	-111.2958	1798
12	BR-07-So	soil				42.2193	-111.2958	1798
12	BR-07-P1	plant	willow	*Salicaceae*	*Salix*	42.2193	-111.2958	1798
12	BR-07-P2	plant	willow	*Salicaceae*	*Salix*	42.2193	-111.2958	1798
13	BR-08-P	plant	aspen	*Salicaceae*	*Populus*	42.1912	-111.4817	1933
14	BR-09-P1	plant	fir	*Pinaceae*	*Abies*	42.1853	-111.5312	2170
14	BR-09-P2	plant	spruce	*Pinaceae*	*Picea*	42.1853	-111.5312	2170
15	BR-10-P	plant	aspen	*Salicaceae*	*Populus*	42.1134	-111.4464	1875
16	BL-01-Se	beach sand				42.0193	-111.2602	1815
16	BL-01-So	soil				42.0194	-111.2599	1811
16	BL-01-P1	plant	aquatic sedge	*Cyperaceae*	*Schoenoplectus*	42.0193	-111.2602	1815
16	BL-01-P2	plant	grass	*Poaceae*		42.0193	-111.2602	1815
17	BL-02-Se	river sediment				41.9201	-111.2543	1892
18	BL-03-Se	lake sediment				41.8573	-111.3627	1807
18	BL-03-P	plant	willow	*Salicaceae*	*Salix*	41.8573	-111.3627	1807
19	BL-04-Se	lake sediment				41.9442	-111.3906	1776
20	BR-11-Se	river sediment				42.1042	-111.4948	1970
20	BR-11-P1	plant	willow	*Salicaceae*	*Salix*	42.1042	-111.4948	1970

20	BR-11-P2	plant	grass	*Poaceae*		42.1042	-111.4948	1970
21	BR-12-P1	plant	spruce	*Pinaceae*	*Picea*	42.0973	-111.5337	2119
21	BR-12-P2	plant	pine	*Pinaceae*	*Pinus*	42.0973	-111.5337	2119
21	BR-12-P3	plant	fir	*Pinaceae*	*Abies*	42.0973	-111.5337	2119
22	BR-13-P1	plant	aster	*Asteraceae*	*Aster*	42.0945	-111.5297	2103
22	BR-13-P2	plant	aster	*Asteraceae*	*Aster*	42.0945	-111.5297	2103
23	BR-14-P	plant	spruce	*Pinaceae*	*Picea*	41.9413	-111.4818	2300
24	BR-15-P1	plant	Artemisia	*Asteraceae*	*Artemisia*	41.9637	-111.5323	2119
24	BR-15-P2	plant	pine	*Pinaceae*	*Pinus*	41.9637	-111.5323	2119
24	BR-15-P3	plant	fir	*Pinaceae*	*Abies*	41.9637	-111.5323	2119
25	BR-16-Se	river sediment				41.8407	-111.8805	1346
25	BR-16-So	soil				41.8407	-111.8805	1346
25	BR-16-P	plant	willow	*Salicaceae*	*Salix*	41.8407	-111.8805	1346